Title: Novel therapeutic targets to mitigate early neuronal dysfunction and cognitive deficits in tauopathy

Authors: Shon A. Koren[1], Matthew J. Hamm[1], Ryan Cloyd[2], Sarah N. Fontaine[2], Emad Chishti[2], Chiara Lanzillotta[3], Fabio Di Domenico[3], Nicholas T. Seyfried[4], Duc Duong[4], David Powell[5], Moriel Vandsburger[6], Anika M.S. Hartz[2], John Koren 3[rd, 1], Jeffrey M. Axten[7], Nicholas J. Laping[7], Jose F. Abisambra[1,*]

Affiliations:

[1]Department of Neuroscience & Center for Translational Research in Neurodegenerative Disease, University of Florida, Gainesville, FL, USA.

[2]Sanders Brown Center on Aging & Department of Physiology, University of Kentucky, Lexington, KY, USA.

[3]Department of Biochemical Sciences, Sapienza University of Rome, Rome, Italy.

[4]Department of Biochemistry and Emory Integrated Proteomics Core, Emory University School of Medicine, Atlanta, GA, USA.

[5]Magnetic Resonance Imaging and Spectroscopy Center, University of Kentucky, Lexington, KY, USA.

[6]Department of Bioengineering, University of California, Berkeley, CA, USA.

[7]GlaxoSmithKline, Research and Development, Collegeville, PA, USA.

*To whom correspondence should be addressed: j.abisambra@ufl.edu

One Sentence Summary: Multi-target kinase inhibition rescues cognitive function in early stage tauopathy mice and reverses proteomic shifts common to Alzheimer's disease in humans.

Abstract: Tauopathies are a group of more than twenty known disorders that involve progressive neurodegeneration, cognitive decline, and pathological tau accumulation. Current therapeutic strategies provide only limited, late-stage symptomatic treatment. This is partly due to lack of understanding of the molecular mechanisms linking tau and cellular dysfunction, especially during the early stages of disease progression. In this study, we treated early stage tau transgenic mice with a multi-target kinase inhibitor to identify novel substrates that contribute to cognitive impairment and exhibit therapeutic potential. Drug treatment significantly ameliorated brain atrophy and cognitive function as determined by behavioral testing and a sensitive imaging technique called manganese-enhanced magnetic resonance imaging (MEMRI) with quantitative R1 mapping. Surprisingly, these benefits occurred despite unchanged hyperphosphorylated tau levels. To elucidate the mechanism behind these improved cognitive outcomes, we performed quantitative proteomics to determine the altered protein network during this early stage in tauopathy and compare this model with the human AD proteome. We identified a cluster of preserved pathways shared with human tauopathy with striking potential for broad multi-target kinase intervention. We further report high confidence candidate proteins as novel therapeutically relevant targets for the treatment of tauopathy.

Introduction

40 Tauopathies, the most common of which is Alzheimer's disease (AD), are a group of
41 neurological disorders defined by the neuropathological accumulation of tau protein that present
42 progressive cognitive dysfunction and brain atrophy. No cure for tauopathies exists, and current
43 treatment strategies are palliative *(1, 2)*. Several clinical trials have targeted toxic tau species
44 through immunotherapies or by inhibiting tau post-translational modifications and fibrillization
45 with mixed results *(1–4)*. However, the disease etiology of tauopathies, AD in particular, are
46 almost certainly multifactorial. A promising strategy to mitigate the complex nature of tauopathies,
47 similar to established approaches for other chronic, progressive diseases, encompass multi-target
48 or combinatorial treatments *(3, 5)*. However, these strategies are limited by requiring a thorough
49 understanding of the cellular perturbations that underly the disease.

50 Modern systems biology approaches provide unparalleled power in investigating the
51 cellular alterations in disease. These tools highlight promising candidate targets for novel
52 therapeutics while elucidating the pathophysiology of the disease. Recent studies focused on the
53 molecular network changes in AD suggest concurrent changes in energy metabolism, immune
54 response, synapse activity, cytoskeletal stability, and RNA metabolism pathways present early in
55 disease progression *(6–8)*. These reports validate decades of research utilizing *in vitro* and *in vivo*
56 disease models. Using these tools, the pathways most closely associated with early cognitive
57 decline and neurodegeneration can be determined and used to assess novel therapeutics.
58 Importantly, these resources have not yet been applied to establish the efficacy of multi-target
59 drugs in mitigating cognitive decline in animal models of tauopathy.

60 Aberrant phosphorylation and kinase signaling is a hallmark of AD and other tauopathies
61 *(8, 9)*. Here, we report the use of a multi-target kinase inhibitor, GSK2606414 or 414, to treat tau
62 transgenic mice in a proof-of-concept study to evaluate whether such strategies can mitigate the

early negative outcomes of tauopathy. This compound potently inhibits multiple tyrosine and serine/threonine kinases at low micromolar concentrations *(10)* and ameliorates phenotypes in a variety of neurological disorder and neurodegenerative models *(11–16)*. The targets of 414 include kinases involved in tauopathy pathogenesis, including protein kinase R-like endoplasmic reticulum kinase, or PERK *(10–12)*, the MAPK cascade *(10)*, receptor-interacting serine/threonine-protein kinase 1, or RIPK1 *(17)*, and KIT *(18)*. We show that brain atrophy and phenotypes of cognitive dysfunction evident in this mouse model of tauopathy are substantially reduced by treatment with 414. Using manganese-enhanced MRI (MEMRI) with parametric mapping, we show that multi-target kinase inhibition rescues deficits in hippocampal calcium activity. The rescue of tauopathy occurs in the absence of changes to toxic, hyper-phosphorylated tau levels and without inhibition of PERK, the target canonically associated with the neuroprotective benefits of 414 *(10, 11)*. We use quantitative proteomics to investigate both the cellular alterations and the networks responsive to multi-target kinase inhibition associated with cognitive rescue in this early stage tauopathic mouse model. Finally, we identify novel candidate proteins that are rescued by drug treatment and are consistent between the tauopathy mouse and human proteome. These analyses identify novel candidate targets for therapeutic intervention in future studies.

Results

Tau transgenic mice exhibit common neurodegenerative features ameliorated by multi-target kinase inhibition

To investigate the pathways responsible for early cognitive impairment in tauopathy and their amenability to treatment with a multi-target kinase inhibitor, we used the rTg4510 tau transgenic mouse model of frontotemporal lobar degeneration (FTLD). The rTg4510 (Tg) mice exhibit well-characterized disease progression driven by the overexpression of P301L human tau

87 primarily in forebrain neurons *(19–21)*. Neurofibrillary tau pathology appears as early as two
88 months, with progressively worsening cognitive impairment detectable as early as two and a half
89 months. Additionally, significant brain atrophy is detectable in this model by 5 months of age (Fig.
90 1A).

91 We treated four-month-old Tg and non-transgenic control (NTg) mice with the multi-target
92 kinase inhibitor GSK2606414 (414) for 30 days. Four-month-old Tg mice display significant tau
93 burden, but they do not present with severe cognitive impairment and therefore provide a
94 therapeutic window amenable to treatment strategies. T2-weighted MRI (Fig. 1B-F) revealed that
95 Tg mice treated with vehicle (Tg + Veh) exhibited an approximately 20% reduction in total brain
96 volume compared with non-transgenic control mice treated with either vehicle (NTg + Veh, **p
97 = 0.0063) or 414 (NTg + 414, **p = 0.0012). Surprisingly, tau transgenic mice treated with 414
98 (Tg + 414) exhibited only a 10% reduction in total brain volume that lacked statistical significance
99 from NTg + Veh control animals (ns, $p > 0.15$).

100 Having observed that 414 treatment decreased brain atrophy in the Tg mice, we then
101 examined if treatment with 414 also rescued cognitive deficits. To analyze changes in neuronal
102 activity *in vivo*, we performed an imaging approach that measures brain function using manganese-
103 enhanced MRI (MEMRI) with parametric mapping *(22, 23)* . MEMRI utilizes manganese as a
104 contrast agent that can flow through calcium channels such as voltage-gated calcium channels *(24–*
105 *26)* and N-methyl-d-aspartate (NMDA) receptors *(27)* that lengthens R1 relaxation rates in tissue
106 *(28)*. When MEMRI is combined with an imaging protocol to quantify the change in R1 relaxation
107 rates over time, or ΔR1, the acquired data reflects calcium dynamics as a measure of neuronal
108 activity in the living brain *(23, 28, 29)*.

109 We previously established that this tau transgenic mouse line exhibits altered calcium
110 homeostasis detected by MEMRI as early as 3mo of age which continues as the mice age *(22)*.
111 Here, we corroborated those findings, identifying altered ΔR1 in 5mo Tg mice (Fig. 2A-D). The
112 strongest differences in ΔR1 observed were found in hippocampal regions such as the dentate
113 gyrus (DG, Fig. 2E) and Cornu ammonis area 1 (CA1, Fig. 2F). In both regions, our experimental
114 Tg + Veh mice exhibited significantly decreased ΔR1 when compared to the control NTg + Veh
115 mice (DG, ***$p = 0.0003$; CA1, *$p = 0.0226$). Tg + 414 treated mice displayed no apparent
116 impairment in calcium activity measured by MEMRI in both regions relative to NTg + Veh mice
117 (DG and CA1, ns) and displayed significant improvement in calcium activity relative to the Tg +
118 Veh animals (DG, **$p = 0.0019$; CA1, *$p = 0.0211$). These findings demonstrate that, in tandem
119 with the changes in total brain volume, treatment with the multi-target kinase inhibitor 414 rescued
120 hippocampal activity deficits in this model.

121 Since calcium dyshomeostasis underlies cognitive impairments in tauopathy *(30)*, we
122 evaluated the effects of 414 in two behavioral paradigms: open field as a measure of anxiety-like
123 phenotype, and Y-maze as a measure of cognition. The open field behavioral paradigm
124 demonstrated a Tg phenotype wherein Tg + Veh mice spent more time in the field periphery than
125 either NTg group (NTg + Veh: **$p = 0.0012$; NTg + 414: ***$p = 0.0001$), suggesting a transgene-
126 dependent anxiety-like behavior (Fig. 3G). Concurrent with our brain volume and calcium
127 signaling findings, Tg mice treated with 414 spent significantly less time in the periphery than Veh
128 treated Tg mice (*$p=0.0260$) and were statistically indistinguishable from either NTg treatment
129 group (ns, $p > 0.15$). In the Y-maze, Tg + Veh mice exhibited decreased novel arm entries (*$p =$
130 0.0365) compared to NTg control mice. Treatment of Tg animals with 414, though statistically
131 indistinguishable from the NTg groups ($p > 0.15$, ns) only partially rescued the number of entries

132 (ns, $p = 0.1095$) compared to vehicle-treated Tg mice (Fig. 2H). Additional Y-maze analysis
133 parameters, such as the total time spent in the novel arm, indicated Tg + Veh mice had reduced
134 performance compared to NTg + Veh mice (*$p = 0.0433$). Again, the Tg + 414 treatment group
135 was statistically indistinguishable from either NTg group (ns, $p > 0.15$) but displayed an
136 incomplete rescue of this phenotype as compared to Tg + Veh mice (ns, $p = 0.0882$) (Supplemental
137 Fig. 1). Consistent with our MEMRI and brain volume data, these data demonstrated that treatment
138 with 414 mitigates the cognitive deficits of early-stage tauopathy in this model.

139 *GSK2606414 rescues functional deficits without altering tau hyper-phosphorylation*

140 Reduction of tau pathology typically correlates and is interpreted as the reason why novel
141 therapeutic strategies improve tauopathy outcomes. Previously, GSK2606414 had been reported
142 to reduce tau pathology by preventing PERK activation and consequent enhancement of GSK3β
143 activity *(11)*. GSK3β phosphorylates tau at sites that are associated with disease *(31)*. To test
144 whether the reduction of tau was responsible for the cognitive rescue in Tg mice, we measured
145 changes in the levels of disease-associated, hyper-phosphorylated tau at the S396/S404 (PHF1)
146 epitope along with total tau levels (Fig. 3A). Quantification of immunoblots indicated that 414 did
147 not modify the levels of PHF1, total tau, nor the relative phosphorylation at the PHF1 epitope (Fig.
148 3B-D). We further measured changes in the levels of active, Y216-phosphorylated and total
149 GSK3β (Fig. 3E) and found that 414 similarly did not modify the levels of activated GSK3β (Fig.
150 3F). These data suggest that the neuroprotective benefits conferred by 414 in these Tg mice are
151 not directly related to changes in tau or phosphorylated tau, but rather through alternative targets.

152 *Functional deficits of early stage tau transgenic mice do not depend on PERK/UPR activation*

153 GSK2606414 was developed as a first-in-class inhibitor of PERK *(10)*. PERK, an ER-
154 associated kinase, functions as part of the unfolded protein response (UPR) by attenuating global
155 translation and dampening the level of incoming nascent proteins in the ER under conditions of
156 ER stress *(32)*. However, long term PERK activation leads to sustained suppression of translation
157 and activation of pro-apoptotic signaling cascades. Previous studies have used 414 to inhibit PERK
158 to rescue or prevent neurodegeneration by limiting the deleterious chronic activation of the UPR
159 *(11, 12, 32)*. We evaluated whether PERK inhibition was a primary factor in the neuroprotective
160 effects of 414 treatment in these early stage Tg mice. Consistent with several reports showing
161 PERK activity does not begin until late-stage tauopathy progression in this model *(11, 33, 34)*,
162 PERK activation (as measured by the phosphorylation of T980) was minimally detected by
163 immunofluorescent stains of the hippocampus and cortex of 5mo Tg mice (Fig. 3G-H). At 8mo,
164 Tg mice had several thousand-fold greater levels of phosphorylated PERK (Fig. 3I-J) which was
165 inhibited by 414 treatment as previously reported (Fig. 3K) *(11)*. We used quantitative real-time
166 PCR gene card arrays to verify our immunofluorescence findings by monitoring transcript levels
167 of genes directly altered by PERK activation. The expression levels of genes downstream of PERK
168 were largely unchanged in the 5mo Tg animals compared to NTg controls, and they were
169 unmodified by 414. These data confirm the absence of strong PERK activity (Fig. 3L). We also
170 measured other mediators of the UPR distinct from the PERK pathway such as ATF6, IRE1, and
171 other eIF2α kinases. Only the transcriptional regulator ATF6 exhibited a significant change in
172 transcript levels in Tg mice, with a reduction of ATF6 mRNA levels in Tg + Veh mice which was
173 Tg mice treated with 414 (Supplemental Fig. 2). PERK reportedly switches preferential substrate
174 phosphorylation in tauopathies between eIF2α and other targets such NRF2, a transcription factor
175 which undergoes nuclear translocation and induces the expression of redox response proteins when

176 phosphorylated by PERK *(35)*. Consistent with our other data, 414 did not alter NRF2 nuclear
177 translocation in Tg model mice (Fig. 3M-N). Considering the off-target effects of kinase inhibitors,
178 and those targeted by 414 beyond PERK at nanomolar and low micromolar concentrations (Table
179 S1), we reasoned that the neuroprotective effect of 414 is likely due to a multi-target response
180 distinct from inhibiting PERK kinase activity.

181 *Quantitative hippocampal proteomics reveals pathways responsible for cognitive decline in early*
182 *stage tauopathy mice*

183 To assess the effects of a compound impacting multiple cellular pathways simultaneously,
184 we turned to quantitative proteomics to identify proteins and pathways most impacted by
185 transgenicity and our test agent, 414. Despite the prevalence of the rTg4510 model in the study of
186 neurodegeneration, no quantitative analysis of the brain proteome in these mice has been reported.
187 To this end, we evaluated the hippocampal proteome of NTg and Tg mice treated with either Veh
188 or 414 (n = 4 per group, all female) using a multiplexed tandem mass tagging (TMT) approach
189 (Fig. 4A). Following protein quantification, batch normalization, and statistical analyses, 337
190 proteins were identified as significantly altered across all group comparisons (FDR adjusted p
191 value < 0.05, Fig. 4B). First, we identified the impact of 414 treatment on proteins in NTg animals
192 (termed: "Drug Effect") and removed these proteins from further analysis. Next, we determined
193 which proteins were altered due to Tg genotype (termed: "Tg Effect") by comparing NTg + Veh
194 vs Tg + Veh samples and specifically excluded any genes known to be dysregulated due to
195 transgene insertion in this model *(36, 37)*. We then identified the proteins that were rescued by 414
196 treatment in the Tg mice: proteins in the "Tg Effect" group that were restored to statistically normal
197 levels in Tg mice (no significant difference from NTg + Veh mice) following treatment with 414
198 (termed: "Drug Rescued"). These groupings are summarized in (Fig. 4C) and representative

199 proteins belonging to each group are shown in (Fig. 4D). Interestingly, ≈67% of the proteins altered
200 in Tg mice were rescued after treatment with 414 (186 out of 276). Importantly and as expected,
201 the human *MAPT* P301L transgene was significantly upregulated in Tg mice and unaffected by
202 414 (Fig. 4E) thus confirming the tau immunoblots and validating the proteomic results.

203 Next, we analyzed the pathway level changes in the 5mo Tg brain proteome. To collapse
204 the altered protein into pathways, we used g.Profiler *(38)* to assess the changes in Reactome *(39)*
205 annotated pathways (FDR adjusted p value < 0.1, Table S2). Cytoscape *(40)* was used to cluster
206 each pathway into larger umbrella networks that were down-regulated (Fig. 4F) or up-regulated
207 (Fig. 4E) in Tg mice. The down-regulated protein network clustered into nine discrete groups,
208 namely: mTOR pathway activity, synaptic activity and long-term potentiation, reactive oxygen
209 species defense, calcium dynamics, vesicle-mediated transport and endocytosis, rho GTPase
210 activity, muscle contraction, RNA metabolism and splicing, as well as aerobic respiration and
211 mitochondrial activity. The number of up-regulated protein networks was considerably larger
212 despite having fewer significantly altered proteins compared to down-regulated proteins. Up-
213 regulated pathways clustered into the following groups: Golgi/ER transport, ion conductance,
214 immune response kinase activity, aerobic respiration and mitochondrial function, axonal and
215 neuritic morphogenesis, neurotransmitter release, amino acid metabolism, heat shock stress
216 response, insulin signaling, rho GTPase activity, cell cycle, Wnt and Hedgehog signaling, as well
217 as gap junctions and plasma membrane.

218 *Multi-target kinase inhibition via GSK2606414 treatment rescues broad proteomic shifts in*
219 *tauopathy*

220 Having identified and mapped the pathway changes in Tg mice, we sought to determine
221 the pathways that were affected by 414 that associated with cognitive rescue. To that end, we

222 repeated clustering analysis of Reactome pathways (FDR adjusted p-value < 0.1) representing
223 "Drug Rescued" proteins that were either initially down-regulated (Fig. 5A) or up-regulated (Fig.
224 5B) in Tg + Veh mice and rescued back toward NTg control levels with 414 treatment. Pathway
225 groups initially down-regulated in Tg + Veh mice and rescued up toward NTg control levels
226 included: aerobic respiration, long-term potentiation, muscle contraction, ion conductance, and rho
227 GTPase activity. Other pathways initially up-regulated in Tg + Veh mice and restored to NTg
228 control levels included: amino acid metabolism, aerobic respiration and mitochondrial function,
229 heat shock stress response, Golgi-ER membrane trafficking, axonal and neuritic morphogenesis,
230 apoptotic protein degradation, cell cycle, gap junction and plasma membrane, immune response
231 kinase activity, ion conductance, NMDA post-synaptic activity, Wnt and Hedgehog signaling, and
232 RNA metabolism and translation.

233 To validate these results, we focused on two distinct cellular processes that were rescued
234 by 414: RNA translation and mitochondrial redox defense. RNA translation was assessed by a
235 novel metabolic labeling method developed to investigate the translational dysregulation of
236 tauopathy *in vivo (34)*. This method involved an intraperitoneal injection of puromycin, a tRNA
237 analog, shortly before death to rapidly label nascent polypeptide chains *(41)*. Anti-puromycin
238 antibodies were then used to probe for proteins that incorporated the puromycin as a direct measure
239 of polypeptide elongation and RNA translation. Anti-puromycin staining of the CA1 region
240 revealed significantly increased translation activity in Tg + 414 (*$p < 0.05$) compared to Tg + Veh
241 mice (Fig. 5C-D). Secondly, since nitroxidative stress is a marker of mitochondrial dysregulation,
242 and it is implicated in the pathogenesis of AD and other tauopathies *(42, 43)*, we measured changes
243 in protein nitration between our animal groups. Immunoblot results identified a significant increase
244 in protein nitration (3-NT) in Tg + Veh animals which was rescued with 414 treatment (Fig. 5E-

245 F). Together, these results validated the pathway level changes that were rescued in Tg mice by
246 treatment with 414.

247 *Early stage tauopathy exhibits common protein alterations targetable by multi-target kinase*
248 *inhibition*

249 Finally, we investigated how the Tg hippocampal proteome compared with human
250 tauopathy to provide a context for our findings in AD. We correlated the 276 proteins altered by
251 "Tg Effect" with two independent proteomic analyses of the human AD brain to identify both
252 model-specific alterations and novel candidate proteins (Table S3). The majority of significantly
253 altered mouse proteins mapped to human homologs (>90%) in both human tauopathy datasets, as
254 expected. First, to account for the disparity in pathology between the tauopathy Tg mouse model
255 and AD, we assessed the consistency of proteomic alterations between Tg mouse and preclinical
256 (or asymptomatic) AD and late-stage AD samples (Fig. 6A). Individuals with asymptomatic AD
257 (Asym AD) included in this analysis exhibited minimal cognitive impairment with moderate to
258 high amyloid plaque frequency, but with low to no cortical tau pathology (Table S4) *(44)*. Late
259 AD samples, however, had significant cognitive impairment and high degrees of amyloid and tau
260 pathology. By identifying the proteins consistent between Tg mice and Asym AD distinct from
261 late AD, we classified which proteins are considered early markers of AD- and tauopathy-specific
262 progression, respectively. We found that 15 of 20 human homologs significantly altered in Asym
263 AD vs healthy control brains were consistently altered in Tg animals (75%; hypergeometric test,
264 ****$p < 0.0001$). Of these 15, nine homolog proteins were rescued by 414 in Tg mice: NUCB1,
265 SNCA, FKBP1A, PKM, YWHAZ, HSPE1, GRPEL1, NDUFB10, and HOMER1. These nine
266 proteins are implicated in other neurodegenerative diseases or cellular processes known to be
267 dysregulated early in tauopathy pathogenesis such as synaptic plasticity, proteostasis, glucose

268 metabolism, and mitochondrial function. Tg mice matched to a greater extent with the late AD
269 proteome, where 30 out of 48 significantly altered proteins were inter-specially consistent (≈63%;
270 hypergeometric test, ****$p < 0.0001$). Of these 30 proteins, 23 homologs were rescued by 414 in
271 Tg mice: NUCB1, NTM, ATOX1, SNCA, ENO1, GJA1, FKBP1A, ATP6V1E1, PKM, STMN1,
272 VSNL1, YWHAZ, HINT1, HPCA, PEPD, ROGDI, PPP1R7, PACSIN1, HSPE1, RTN1,
273 NDUFB5, DMTN, and HOMER1. These proteins function in pathways rescued by 414 in Tg mice,
274 namely aerobic respiration/glucose metabolism, mitochondrial function, endocytosis and
275 trafficking, immune system activation, signaling cascades. Interestingly, several proteins were
276 found consistent across disease staging: NUCB1, SNCA, FKBP1A, PKM, YWHAZ, HSPE1,
277 HOMER1. Since each of these were rescued by 414 in Tg mice, they may be important candidate
278 proteins to consider for future studies.

279 Considering that the proteome in late-stage neurodegenerative diseases may relate more to
280 widespread brain organ failure and may not be a specific response to any one disease *(45)*, we
281 investigated how the Tg proteome matched the protein alterations in AD and another chronic,
282 degenerative neurodegenerative disease, Parkinson's disease (PD) *(46)*. We applied a similar
283 approach used with asymptomatic and late stage AD, wherein we analyzed whether proteins found
284 altered in the Tg hippocampal proteome were consistently altered in AD or PD (Fig. 6B).
285 Interestingly, Tg animals and PD brains did not share consistently altered homologous proteins,
286 suggesting a tauopathy specific effect. Of the 39 significantly altered proteins found in AD, 26 had
287 homologs consistently changed in Tg animals (≈67%; hypergeometric test ****$p<0.0001$), and 16
288 were rescued by 414: AKAP5, STMN3, EEF1B2, FKBP1A, ATP6V1E1, NDUFS6, CYCS,
289 CPLX1, HINT1, PACSIN1, CIAPIN1, RHEB, DDAH1, NDUFB10, ALDH6A1, PIN1. These
290 proteins function in aerobic respiration/glucose metabolism, RNA translation, apoptosis, immune

291 system activation, reactive oxygen and nitrogen species defense, membrane trafficking, and
292 neurotransmitter release.

293 Four proteins were consistently shared across both late AD datasets with mouse homologs rescued
294 by 414 in Tg mice (Fig. 6C). These high-confidence, novel candidate proteins are PACSIN1,
295 FKBP1A, ATP6V1E1, and HINT1. Future studies aimed at investigating the therapeutic impact
296 of targeting one or all these proteins is currently underway.

297

298 **Discussion**

299 Tauopathy brains are characterized by aberrant aggregation of a variety of tau conformers,
300 which include hyperphosphorylated tau species. To reduce tau hyperphosphorylation with the goal
301 of limiting tau pathogenesis, clinical trials using small molecule kinase inhibitors have
302 predominantly targeted either individual kinases or whole kinase families with some success *(47–*
303 *50)*. Nilotinib, a multi-family kinase inhibitor, was used in a recently completed Phase II clinical
304 trial in which it reduced hippocampal volume loss, cognitive decline, and phosphorylated tau levels
305 in early to moderate AD patients *(51)*. The compound targets multiple tyrosine kinase families
306 *(52)*, strongly supporting the therapeutic potential of broad kinase inhibitors in treating
307 tauopathies. Despite these encouraging outcomes, the precise pathways targeted by Nilotinib and
308 other kinase inhibitors are unknown. Given the numerous roles of kinases in biological processes,
309 identification of discrete targets that can be chemically regulated, as well as the mechanisms that
310 contribute to neuronal dysfunction in tauopathies, will likely improve the chances for success in
311 the clinic.

312 Here, we uncover critical biological processes that contribute to neurotoxic processes
313 driving tauopathies using a multi-family kinase inhibitor, GSK2606414. In doing so, we

314 demonstrate the potential to mitigate the negative functional consequences of tauopathy without
315 altering tau hyper-phosphorylation. We treated early stage rTg4510 tau transgenic mice and,
316 compared to previous studies, we firmly established cognitive and molecular benefits of broad-
317 based kinase inhibition. With TMT quantitative proteomics, we identified biological processes that
318 are affected in the tauopathy mice and rescued by the compound. Finally, we cross-reference our
319 findings to human AD and PD brain proteomic data to narrow our results to high confidence unique
320 targets for future study. This approach revealed four distinct proteins associated with cognitive
321 decline in human tauopathy with strong therapeutic potential.

322 GSK2606414 ameliorates molecular underpinnings of neurodegeneration including
323 neuronal loss, cognitive dysfunction, and pathological protein accumulation in a variety of disease
324 models *(11–16, 18)*. These studies established that the benefits of GSK2606414 were conferred by
325 inhibition of its primary target, PERK, which was upregulated in disease. While PERK is active
326 in the rTg4510 tau transgenic model, this does not occur until after 6mo *(11, 33)*. By treating
327 rTg4510 mice from 4-5mo, a time point in which PERK levels not activated, our study identified
328 numerous PERK-independent pathways targeted by GSK2606414 that elicited rescue from toxic
329 outcomes in tauopathy. This has important implications for data interpretation of this and previous
330 studies.

331 The mechanism by which GSK2606414 confers benefits implicates multiple but
332 identifiable and targetable pathways. While GSK2606414 is a potent PERK inhibitor, the
333 concentration needed to reduce PERK activity *in vivo* also inhibits many other significant kinases
334 *(12)*. In fact, GSK2606414 targets are numerous and have substantial implications in promoting
335 neurodegeneration *(10, 17, 18)*. While GSK2606414 inhibits many tyrosine kinases shared with
336 Nilotinib and dozens of others involved in pathways mediating neurodegenerative diseases *(10)*,

337 our broad approach to also inhibit serine and threonine kinases casts a wider net to identify
338 phosphorylation-dependent events linked to tau pathogenesis.

339 We found that measures of early neurodegeneration and cognitive decline in rTg4510 mice
340 were consistent with other studies. Volumetric T2-weighted MR imaging revealed brain atrophy
341 in line with other studies in the same transgenic model *(19, 20, 53, 54)*. Neuronal functional deficits
342 were assessed using MEMRI, a functional imaging approach that uses manganese to approximate
343 calcium homeostasis *(23)*. Hippocampal decreases in ΔR1, a measurement of manganese retention
344 over time, supported other studies identifying tau-associated suppression of neuronal calcium
345 activity in the same model of tauopathy *(55)*. Behavioral phenotypes involving hippocampal
346 activity were also impaired at this stage in rTg4510 mice, supporting other studies in this model
347 *(20, 56, 57)* and MR imaging indications of brain dysfunction and degeneration present in this
348 study. Importantly, the functional deficits in this model appear to be tau-dependent since transgenic
349 mice fed doxycycline to suppress tau transgene expression exhibited rescued cognitive and
350 behavioral activity *(19, 20, 55, 56)*. While transgenicity in rTg4510 mice disrupts the genetic
351 expression of several genes *(37)*, these studies suggest that the functional deficits in this model are
352 largely tau dependent.

353 To evaluate the protein network changes behind this functional rescue, we completed the
354 first deep proteomic profiling of the brain in rTg4510 mice by quantitatively measuring the
355 hippocampal proteome. Many of the pathways affected by disease in this early stage of rTg4510
356 mice overlap with altered pathways in AD brain such as glucose metabolism, immune response,
357 synaptic activity, and RNA metabolism, highlighting the similarity between this model and human
358 tauopathy *(6–8, 44)*. The largest alterations in kinase pathway activities were the MAPK cascade,
359 which is consistent with the involvement of MAPK in human tauopathies *(8)*. Pathways involving

360 regulation of calcium dynamics were also down-regulated which supports the deficits in calcium-
361 related activity measured by MEMRI. Pathways involved in muscle contraction were also
362 dysregulated in the rTg4510 hippocampus, which is consistent with locomotor alterations reported
363 in this model *(56)* and other mouse models of tauopathy *(58)*. Interestingly, pathways relating to
364 cell cycle re-entry were altered in rTg4510 mice. These data support the evidence that cell cycle
365 dysregulation occurs as a result of, and a potential promoter for, tau pathogenesis as seen in human
366 AD brain and mouse models of tauopathy *(59–61)*. Comparing our proteomic results with a study
367 of proteostatic dysfunction and protein aggregation in rTg4510 reveals no apparent correlation of
368 protein abundance between soluble and insoluble fractions *(62)*. These studies suggest that our
369 proteomic findings reflect alterations in expression and degradation rather than a protein shift
370 toward insolubility.

371 Treatment with GSK2606414 broadly affected the hippocampal proteome of rTg4510 mice
372 and only minimally affected non-transgenic controls. Many pathways critical for neuronal health
373 altered in human tauopathies were rescued in 414-treated tau transgenic mice. This provides
374 further support for the multi-target engagement of GSK2606414. Multiple kinase-related pathways
375 were rescued in transgenic animals treated with GSK2606414, such the MAPK and Wnt signaling
376 cascades responsible for downstream kinase regulation and tau hyper-phosphorylation *(63)*. These
377 results were comparable with a recent report on the phospho-proteome changes in AD suggesting
378 the broad activation of the MAPK cascade in tauopathy *(8)*. We verified the proteomic alterations
379 found in this study by confirming both translation elongation and mitochondrial redox
380 accumulation were altered in tau transgenic mice and reduced with 414 treatment (Fig. 5C-F).
381 Furthermore, mass spectrometry quantification of human P301L tau revealed no significant
382 alteration of total tau levels with 414 treatment which matched our immunoblot results.

383 Given the congruent pathway-level results between rTg4510 mice and human tauopathy
384 studies, we searched for novel candidate targets that were associated with rescued cognitive
385 function with GSK2606414 treatment. We compared our results with quantitative proteomic cases
386 of AD as no other deep, high sample number proteomic investigation of another tauopathy has
387 been reported. To focus on the impact of tau pathology, we assessed the correlation between
388 cortical proteomic results from cases of asymptomatic AD which exhibit amyloid pathology, but
389 no tau pathology in the cortex, along with late stage AD cases *(44)*. As expected, more proteins
390 were consistent between rTg4510 mice and late AD than asymptomatic cases. However, a
391 considerable number of proteins matched with asymptomatic AD and late stage AD, suggesting
392 that these targets may relate to an early vulnerability which progressively declines over disease
393 course. These changes were specific to tauopathy as no protein was consistent with the PD
394 proteome. Interestingly, alpha-synuclein was down-regulated in transgenic mice and rescued with
395 GSK2606414 treatment earlier in this model than reported elsewhere *(64, 65)*. Since decreased
396 alpha-synuclein monomer levels are associated with their pathological oligomerization and
397 pathological accumulation *(66, 67)*, this early involvement supports a role of for alpha-synuclein
398 in the pathophysiology of tauopathy. Overlapping the proteins consistent in both AD datasets with
399 data from transgenic mice revealed four novel, high-confidence candidates that were associated
400 with cognitive decline and drug-mediated multi-target kinase inhibition: PACSIN1, FKBP1A,
401 ATP6V1E1, and HINT1.

402 The neuronal protein PACSIN1 participates in endocytosis *(68–70)* and directly interacts
403 with tubulin to promote microtubule formation *(71)*. There is evidence for direct tau-PACSIN1
404 binding, suggesting that this interaction impinges upon tau's capacity to bind microtubules *(72)*.
405 Network analyses of AD brain identified PACSIN1 as a hub microtubule regulator and a

406 cerebrospinal fluid marker altered in disease *(6, 44)*. Thus, PACSIN1 represents a protein with a
407 direct link to tauopathy that could perturb cellular trafficking and tau/microtubule stability.

408 The peptidyl-prolyl *cis-trans* isomerase (PPIase) FKBP1A promotes protein folding and
409 trafficking *(73)*. Along with other related PPIases such as FKBP51 *(74–79)*, FKBP1A modifies
410 tau's structure at the proline-rich region. Perturbation of protein quality control and trafficking
411 mechanisms is a nearly ubiquitous feature of proteinopathy neurodegenerative diseases, with these
412 deficiencies often cited as a crucial step in disease cascades that lead to protein mis-folding and
413 aggregation *(80, 81)*. In addition, FKBP1A activity enhances alpha-synuclein aggregation into
414 Lewy body inclusions in PD *(82–86)*. FKBP1A associates with tau pathology in neurofibrillary
415 tangles, suggesting that the protein may play a role in AD pathogenesis *(87)*. Of note, PIN1,
416 another PPI, was similarly down-regulated in late AD brain and was rescued by GSK2606414 in
417 Tg animals in this study. FKBP1A has also been implicated in calcium regulation in myocytes and
418 neuronal signaling *(88, 89)*. Importantly, FKBP1A was the only protein found altered in early AD
419 and late AD in our analyses, suggesting that it may be a useful target to disrupt disease
420 pathogenesis. While the full involvement of FKBP1A in proteostasis and calcium activity is
421 unresolved, there is increasing evidence of its importance in neurodegenerative diseases.

422 *ATP6V1E1* encodes the E1 subunit of the V1 domain of the V-type proton ATPase (V-
423 ATPase), or ATP6VE1. V-ATPase participates in numerous physiological processes involved in
424 tauopathy including glucose metabolism, membrane trafficking, protein degradation, and vesicular
425 acidification *(90)*. Our data indicate that murine ATP6VE1 is reduced in Tg mice and its human
426 homolog down-regulated in both AD tissue sets (Fig. 6). Thus, ATP6V1E1 function may
427 deteriorate with disease progression, despite a clear role for the protein in neurodegenerative
428 disease.

429 HINT1, or histidine triad nucleotide-binding protein 1, was originally described as a
430 protein kinase regulator, but has more recently been implicated in regulation of G protein coupled
431 receptors, or GPCRs, as well as transcription factors that influence Wnt/beta-catenin signaling
432 *(91–94)*. HINT1 has been implicated in many neuropsychiatric disorders including schizophrenia,
433 mood disorders, and drug addiction *(95)*. In Schizophrenia, HINT1 is downregulated in both the
434 dorsolateral prefrontal cortex and prefrontal cortex *(96, 97)*, which mirror its abundance in AD.
435 While HINT1 is not classically associated with neurodegenerative disease, it is possible that
436 HINT1 plays a large role in the molecular mechanisms of neuropsychiatric symptoms present in
437 dementia and in other neurological disorders.

438 Taken together, our pre-clinical study contributes two major findings. First, we identify
439 discrete pathways contributing to cognitive changes in tauopathy and highlight four unique
440 proteins associated with cognitive rescue with strong therapeutic potential. Further work
441 investigating the novel targets identified in this study could discover better targets amenable to
442 pharmacological intervention and novel involvement in tauopathy. Second, we demonstrate that
443 broad, multi-family kinase inhibition can be a useful tool to mitigate the molecular and functional
444 decline in tauopathy. Since extensively multi-targeted approaches meet safety challenges in the
445 clinic, the development of compounds that selectively target key kinase cascades at the same time
446 could greatly benefit combinatorial therapies for the treatment of tauopathy. Studies combining
447 FDA-approved selective kinase inhibitors may be beneficial toward advancing possible
448 therapeutic strategies.

449

450 **Materials and Methods**

451 *Animals*

452 All animal studies were approved by the University of Kentucky's Institutional Animal Care and
453 Use Committee (IACUC) and abided by that committee's policies on animal care and use in
454 accordance with the Guide for the Care and Use of Laboratory Animals, the Animal Welfare
455 Regulations Title 9 Code of Federal Regulations Subchapter A, "Animal Welfare," Parts 1–3, and
456 the Public Health Service Policy on Humane Care and Use of Laboratory Animals. Mice were kept
457 in standard housing on a 12h light/dark cycle and received food and water *ad libitum*. The tau
458 transgenic (rTg4510) and parental mice were maintained and genotyped as described previously
459 *(20)* and were maintained on mixed FVB and 129S6 backgrounds. Mice of both sexes were used
460 in experiments unless otherwise stated.

461 *Treatment with GSK2606414*

462 The multi-target inhibitor GSK2606414 (GlaxoSmithKline) was suspended in vehicle (0.5%
463 hydroxypropylmethyl cellulose + 0.1% Tween-80 in water at pH 4.0) to a dosage of 50 mg/kg, as
464 previously described *(12)*. Prior to treatment, all mice were handled for 10 minutes twice a day to
465 acclimate the animals for gavage. Unless otherwise stated, four-month-old rTg4510 and non-
466 transgenic mice were treated with GSK2606414 or vehicle for 30 days.

467 A total of 100 mg/kg GSK2606414 was delivered by oral gavage once (100 mg/kg) or twice a day
468 (50 mg/kg each separated by 10-12 hours). Mice were weighed to ensure precise dosing prior to
469 each treatment. Daily weight records were carefully monitored due to the potential of irritating the
470 esophagus and previous reports of GSK2606414-mediated weight loss *(12)*. Animals that lost more
471 than 20% of starting body weight were excluded from the study (Supplemental Fig. 3). These
472 animals corresponded to mice in both vehicle and GSK2606414 groups, indicating that weight loss
473 was not due to the compound.

474 *Tissue Preparation*

475 Mouse brains were harvested as previously described *(33)*. Briefly, mice were irreversibly
476 anesthetized using isoflurane and transcardially perfused with 0.9% saline. The right brain
477 hemisphere was drop-fixed in 4% para-formaldehyde for immunohistochemistry. The left
478 hemisphere was microdissected, snap frozen in liquid nitrogen, and stored at -80°C until
479 homogenization. For Western blot analysis, brains were weighed, and homogenization buffer
480 (1:100 Protease Inhibitor, Calbiochem; 1:100 Phosphatase Arrest II, G Biosciences; 1:100
481 Phosphatase Arrest III G Biosciences; 100µM PMSF; in 1x RIPA, Thermo) was added to a final
482 concentration of 10% (w/v). Samples were homogenized using a using a small electronic pestle
483 (VWR). Samples were then centrifuged at 4°C at 13,000xg for 15 minutes. Protein concentration
484 was established using the bicinchoninic acid (BCA) assay (ThermoScientific).

485 *Protein analysis of brain homogenates*

486 Western blots were performed as previously described *(33)*. Briefly, proteins were separated via
487 SDS-PAGE, transferred to PVDF membranes, blocked in 5% (w/v) milk-TBS for 1 hour, and then
488 incubated in primary antibody overnight at 4°C. Primary antibodies diluted in 5% (w/v) milk-TBS
489 were as follows: PHF1 1:1000 (Peter Davies), total tau 1:1000 (H150, SantaCruz), pY216-GSK3β
490 1:1000 (Abcam), total GSK3β 1:1000 (Cell Signaling Technologies), 3-NT (1:500, Santa Cruz),
491 4-HNE 1:1000 (EMD Millipore) and GAPDH and actin for loading controls (1:1000, Cell
492 Signaling Technologies). Different loading controls were used throughout experiments to ensure
493 optimal normalization despite non-specific antibody binding and species reactivity. HRP-
494 conjugated secondary antibodies to mouse or rabbit IgG (Southern Biotech and ThermoScientific)
495 were used at a 1:1000 dilution where appropriate. Bands were visualized using ECL

496 (ThermoScientific). Image quantification was performed using ImageJ, normalized to loading
497 controls.

498 *Open Field Test*

499 Open field-testing was performed in the University of Kentucky Rodent Behavior Core. All testing
500 was performed at the same time of day for each cohort. Animals were acclimated to testing room
501 30 minutes prior to testing. Open field-testing was done with the automated Photobeam Activity
502 System (PAS) with Flexfield Animal Activity System (San Diego Instruments, Inc. San Diego)
503 coupled to a computer used to eliminate human interaction and bias. Each animal was placed into
504 the middle of the open field, facing away from the experimenter and exploratory behavior recorded
505 for 30min. The chamber was cleaned with 10% ethanol between tests to eliminate olfactory cues
506 from previous animals. The time mice spent in the peripheral areas were recorded in six, 5-min
507 intervals and is reported by normalizing to time spent in the first 5-min window. Recordings were
508 taken using EthoVision XT and reviewed by two blinded investigators. Several cohorts were tested
509 independently over periods of months, but each animal was tested on the 21st day of treatment.

510 *Y-maze*

511 Forced alternation test was performed according to a previously published protocol (30). A
512 symmetrical Y-maze (Stoelting Co, Wood Dale, IL, USA) with grey Perspex® walls and a grey
513 steel bottom (arms: 35 cm long, 5 cm wide, 10 cm high) was used for the test. The light in the
514 testing area was kept at 30±5 lux, the test was performed at room temperature (23± 2°C). Mice
515 were handled for 5 days (5min/day/mouse) before testing. During the 5 min sample trial (T1), mice
516 were allowed to explore two arms of the Y-maze, the third arm was blocked. The mice were placed
517 into the end of the start arm facing the wall, away from the center. After completion of the sample

518 trial, each mouse was returned to its home cage for 30 min. During the test trial (T2), the block in
519 arm 3 was removed and the mouse was allowed to explore the entire maze for 5 min. In between
520 animals and trials, the maze was cleaned with Quatricide® solution to prevent odor cues. Total
521 duration and number of entries into open arms is reported.

522 *Manganese-enhanced magnetic resonance imaging (MEMRI)*

523 All MRI procedures were performed in accordance with the University of Kentucky MRISC
524 IACUC Protocol. Brain volume was calculated from T2 images based on manual tracing of the
525 brain. Manganese chloride (30mM) prepared in saline was delivered to mice via intraperitoneal
526 injection (66 mg/kg). All MR imaging was performed on a horizontal bore 7T Bruker ClinScan
527 magnet (Bruker, Ettlingen, Germany) using a cylindrical volume coil for excitation and a cryocoil
528 for detection. In preparation for imaging, animals are anesthetized using isoflurane (3-5%) in
529 oxygen at a rate of 0.5-1.0 L/min and maintained using 1-3% isoflurane in oxygen. Body
530 temperature was maintained using circulating water, and vital signs (core temperature and
531 respirations) were monitored using a physiological monitoring system SA Instruments Inc. (SAI,
532 Stony Brook, New York). When applicable, MEMRI was performed after behavioral testing to
533 reduce stress-related confounds in behavioral test results.

534 Look-locker imaging was performed following non-selective spin inversion in one slice of the
535 hippocampus. Fifty images were acquired following inversion with image spacing of 100ms (total
536 sequence repetition time of 5s) to fully sample the T1-relaxation curve. Additional image
537 parameters included TR/TE = 5500/1.9, Matrix = 128 x 128, number of averages = 3, field of view
538 = 17mm x 17mm x 0.7mm. T2-weighted images were acquired covering the entire brain
539 (excluding the cerebellum and olfactory bulb) using a turbo-spin echo sequence with TR/TE =
540 3360/42, Slices = 21, Matrix = 448 x 336, number of averages = 2, field of view = 25mm x 25mm

541 x 0.5mm. The imaging procedures for scanning one mouse were completed in 45min. Imaging was
542 performed prior to the injection of $MnCl_2$ (baseline) and repeated at 6h post-injection. Image
543 mapping and analysis was performed in MATLAB (Mathworks, Nattic, MA, USA). Images from
544 the Look-Locker series were used to reconstruct voxel-by-voxel signal relaxation curves which
545 were fit to the equation S(t) = So(1-2*exp(-R1*T1)), where S(t) represents the signal at a given
546 inversion time (TI), So represents the steady state signal at maximal T1, and R1 represents the
547 longitudinal relaxation rate. Regions of interest (DG, CA1, CA1, CA3, and superior medial cortex)
548 were identified using the Allen Brain Mouse Atlas. Within each the change in R1 relaxation rates
549 (ΔR1) before and after $MnCl_2$ exposure was calculated as:

550 $$\Delta R_1 = R1_{6h} - R1_{baseline}$$

551 *Quantitative real-time RT-PCR gene card arrays*

552 Total RNA was extracted from snap frozen hippocampal tissues using TRI reagent solution
553 (Ambion) following the manufacturer's protocol. RNA was quantified using a BioTech
554 spectrophotometer and cDNA was generated using SuperScript IV reverse transcriptase
555 (Invitrogen). Real-time RT-PCR was performed using a TaqMan custom Array (Life
556 Technologies) according to manufacturer's instructions. Gene card array was designed to evaluate
557 changes in the expression of genes delineated in Figure 4. Gene expression was evaluated by
558 normalizing to GAPDH and 18S expression as internal controls. The real-time values for each
559 sample were averaged and evaluated using the comparative CT (cycle time) method.

560 *Protein Extraction and Quantification for Proteomics*

561 Microdissected hippocampal mouse tissue were processed for protein extraction which were
562 prepared according to *(98)* with the following modifications. Briefly, samples were ground in

563 liquid nitrogen into fine powder and incubated in extraction buffer (0.1 M Tris-HCl pH 8.8, 10
564 mM EDTA, 0.2 M DTT, 0.9 M sucrose), continued by grinding in a fume hood, and then the
565 extract was agitated for 2 hrs at room temp. After washing twice with 0.1 M ammonium acetate in
566 methanol and twice with 80% acetone, the dried pellet was dissolved with 50mM ammonium
567 bicarbonate buffer. The mixtures were cooled on ice before centrifugation (4°C) for 20 min at
568 12,000 g. The soluble proteins were performed using an EZQ Protein Quantitation Kit (Invitrogen,
569 Carlsbad, CA, USA) with the SoftMax Pro Software v5.3 (Molecular Devices, Downingtown, PA,
570 USA).

571 *Protein Extraction, Digestion, TMT Labeling, and LC-MS/MS*

572 Proteins were dissolved in protein buffer (8M Urea, 50 mM Tris-HCl (pH 8.0), 50 mM
573 triethylammonium bicarbonate, 0.1% SDS (w/v), 1% Triton-100 (w/v), 1 mM PMSF, 10 μg/ml
574 leupeptin, 1% phosphatase inhibitor cocktail 2 and 3 (v/v)). For each sample, a total of 50 μg of
575 protein were reduced, alkylated, trypsin-digested, and labeled according to the manufacturer's
576 instructions (Thermo Scientific). For each mass-spectrometer batch, late-stage 8mo transgenic
577 tissue were labeled with TMT tags 126 and 127N, non-transgenic mice treated with 414 were
578 labeled with TMT tags 128C and 129N, non-transgenic mice treated with vehicle were labeled
579 with TMT tags 128C and 129N, transgenic mice treated with 414 were labeled with 129C and
580 130N, transgenic mice treated with vehicle were labeled with 130C and 131N, and a mixed-sample
581 internal batch was labeled with 131C. Labeled peptides were desalted with C18-solid phase
582 extraction and dissolved in strong cation exchange (SCX) solvent A (25% (v/v) acetonitrile, 10
583 mM ammonium formate, and 0.1% (v/v) formic acid, pH 2.8). The peptides were fractionated
584 using an Agilent HPLC 1260 with a polysulfoethyl A column (2.1 × 100 mm, 5 μm, 300 Å;
585 PolyLC, Columbia, MD, USA). Peptides were eluted with a linear gradient of 0–20% solvent B

586 (25% (v/v) acetonitrile and 500 mM ammonium formate, pH 6.8) over 50 min followed by ramping
587 up to 100% solvent B in 5 min. The absorbance at 280 nm was monitored and a total of 19 fractions
588 were collected. The fractions were lyophilized, desalted, and resuspended in LC solvent A (0.1%
589 formic acid in 97% water (v/v), 3% acetonitrile (v/v)). A hybrid quadrupole Orbitrap (Q Exactive)
590 MS system (Thermo Fisher Scientific, Bremen, Germany) was used with high energy collision
591 dissociation (HCD) in each MS and MS/MS cycle. The MS system was interfaced with an
592 automated Easy-nLC 1000 system (Thermo Fisher Scientific, Bremen, Germany). Each sample
593 fraction was loaded onto an Acclaim Pepmap 100 pre-column (20 mm × 75 μm; 3 μm-C18) and
594 separated on a PepMap RSLC analytical column (250 mm × 75 μm; 2 μm-C18) at a flow rate at
595 350 nl/min during a linear gradient from solvent A (0.1% formic acid (v/v)) to 30% solvent B
596 (0.1% formic acid (v/v) and 99.9% acetonitrile (v/v)) for 95 min, to 98% solvent B for 15 min, and
597 hold 98% solvent B for additional 30 min. Full MS scans were acquired in the Orbitrap mass
598 analyzer over m/z 400–2000 range with resolution 70,000 at 200 m/z. The top ten most intense
599 peaks with charge state ≥ 3 were fragmented in the HCD collision cell normalized collision energy
600 of 28%, (the isolation window was 2 m/z). The maximum ion injection times for the survey scan
601 and the MS/MS scans were 250 ms, respectively and the ion target values were set to 3e6 and 1e6,
602 respectively. Selected sequenced ions were dynamically excluded for 60 sec.

603 Raw data files obtained from the Orbitrap Fusion were processed using Proteome Discoverer™
604 (version 2.3). MS/MS spectra were searched against the UniProt mouse proteome database
605 downloaded Dec 4, 2019 with 63369 total sequences including the sequence for 0N4R P301L tau
606 mutant cDNA. The SEQUEST HT search engine was used and parameters were the following:
607 fully-tryptic specificity; maximum of two missed cleavages; minimum peptide length of 6; fixed
608 modifications for TMT tags on lysine residues and peptide N-termini (+ 229.162932 Da) and

609 carbamidomethylation of cysteine residues (+ 57.02146 Da); variable modifications for oxidation
610 of methionine residues (+ 15.99492 Da); phosphorylation of serine, threonine and tyrosine (+
611 79.9663 Da); precursor mass tolerance of 20 ppm; fragment mass tolerance of 0.05 Daltons.
612 Percolator was used to filter peptide spectral matches (PSM) and peptides to a false discovery rate
613 (FDR) of less than 1% using target-decoy strategy. Following spectral assignment, peptides were
614 assembled into proteins and were further filtered based on the combined probabilities of their
615 constituent peptides to a final FDR of 1%. In cases of redundancy, shared peptides were assigned
616 to the protein sequence in adherence with the principles of parsimony. Reporter ions were
617 quantified from MS2 scans using an integration tolerance of 20 ppm with the most confident
618 centroid setting.

619 Each MS batch protein abundance value was normalized to the internal standard (131C)
620 abundance, enabling batch-corrected analysis across groups. The criteria for protein inclusion in
621 statistical analysis were that each protein must i) be present in all samples, ii) have a global FDR
622 < 0.05, iii) contain at least one unique peptide, and iv) be an annotated master protein. These
623 filtering criteria reduced the total amount of unique protein hits to 24,149 peptides and 1099
624 proteins. Normalized abundance ratios of selected proteins were loaded into R (3.6.2) for
625 processing. Significant differential expression of proteins between samples was determined as $p <$
626 0.05 using unpaired Welch's t-test with FDR multiple-comparisons correction. No fold change
627 (FC) cutoff was used as TMT-labeled tagging and subsequent analysis is subject to ratio
628 compression *(99)*. Reactome pathway *(39)* changes were assessed using gProfiler *(38)* were used
629 against total mouse protein coding background. Significant Reactome pathways (FDR adj. p value
630 < 0.10) were loaded into Cytoscape for clustering analysis *(40)*.

631 *Immunofluorescence*

632 Immunofluorescence (IF) was performed as previously described *(33, 100)*. Primary antibodies:
633 pPERK (1:250, SantaCruz) and NRF2 (1:250; Abcam).

634 *Statistical Analysis*

635 Statistical analyses for all data apart from proteomics were performed using GraphPad Prism 8
636 (Graph Pad Software, Inc. La Jolla, CA, USA). Results are shown as the mean ± standard error or
637 standard deviation as described in each figure. Single-variate data were analyzed using unpaired
638 Student's t-test. Multi-variate data were analyzed with one-way or two-way ANOVA where
639 appropriate, corrected for multiple comparisons with Tukey post-test analysis unless otherwise
640 stated. A value of $p < 0.05$ was considered statistically significant except for Reactome pathway
641 analyses which used an FDR-adjusted p value cutoff of 0.10.

642 **References**

643 1. S. Jadhav, J. Avila, M. Schöll, G. G. Kovacs, E. Kövari, R. Skrabana, L. D. Evans, E. Kontsekova,
644 B. Malawska, R. de Silva, L. Buee, N. Zilka, A walk through tau therapeutic strategies, *Acta*
645 *Neuropathologica Communications* **7**, 22 (2019).

646 2. M. R. Khanna, J. Kovalevich, V. M.-Y. Lee, J. Q. Trojanowski, K. R. Brunden, Therapeutic
647 Strategies for the Treatment of Tauopathies: Hopes and Challenges, *Alzheimers Dement* **12**,
648 1051–1065 (2016).

649 3. L.-K. Huang, S.-P. Chao, C.-J. Hu, Clinical trials of new drugs for Alzheimer disease, *Journal of*
650 *Biomedical Science* **27**, 18 (2020).

651 4. A. L. Boxer, A. E. Lang, M. Grossman, D. S. Knopman, B. L. Miller, L. S. Schneider, R. S. Doody,
652 A. Lees, L. I. Golbe, D. R. Williams, J.-C. Corvol, A. Ludolph, D. Burn, S. Lorenzl, I. Litvan, E. D.
653 Roberson, G. U. Höglinger, M. Koestler, C. R. Jack, V. Van Deerlin, C. Randolph, I. V. Lobach, H.
654 W. Heuer, I. Gozes, L. Parker, S. Whitaker, J. Hirman, A. J. Stewart, M. Gold, B. H. Morimoto, AL-
655 108-231 Investigators, Davunetide in patients with progressive supranuclear palsy: a
656 randomised, double-blind, placebo-controlled phase 2/3 trial, *Lancet Neurol* **13**, 676–685
657 (2014).

658 5. R. R. Ramsay, M. R. Popovic-Nikolic, K. Nikolic, E. Uliassi, M. L. Bolognesi, A perspective on
659 multi-target drug discovery and design for complex diseases, *Clinical and Translational Medicine*
660 **7**, 3 (2018).

661 6. E. C. B. Johnson, E. B. Dammer, D. M. Duong, L. Ping, M. Zhou, L. Yin, L. A. Higginbotham, A.
662 Guajardo, B. White, J. C. Troncoso, M. Thambisetty, T. J. Montine, E. B. Lee, J. Q. Trojanowski, T.
663 G. Beach, E. M. Reiman, V. Haroutunian, M. Wang, E. Schadt, B. Zhang, D. W. Dickson, N.
664 Ertekin-Taner, T. E. Golde, V. A. Petyuk, P. L. De Jager, D. A. Bennett, T. S. Wingo, S. Rangaraju, I.
665 Hajjar, J. M. Shulman, J. J. Lah, A. I. Levey, N. T. Seyfried, Large-scale proteomic analysis of
666 Alzheimer's disease brain and cerebrospinal fluid reveals early changes in energy metabolism
667 associated with microglia and astrocyte activation, *Nat. Med.* **26**, 769–780 (2020).

668 7. E. C. B. Johnson, E. B. Dammer, D. M. Duong, L. Yin, M. Thambisetty, J. C. Troncoso, J. J. Lah,
669 A. I. Levey, N. T. Seyfried, Deep proteomic network analysis of Alzheimer's disease brain reveals
670 alterations in RNA binding proteins and RNA splicing associated with disease, *Mol*
671 *Neurodegener* **13**, 52 (2018).

672 8. B. Bai, X. Wang, Y. Li, P.-C. Chen, K. Yu, K. K. Dey, J. M. Yarbro, X. Han, B. M. Lutz, S. Rao, Y.
673 Jiao, J. M. Sifford, J. Han, M. Wang, H. Tan, T. I. Shaw, J.-H. Cho, S. Zhou, H. Wang, M. Niu, A.
674 Mancieri, K. A. Messler, X. Sun, Z. Wu, V. Pagala, A. A. High, W. Bi, H. Zhang, H. Chi, V.
675 Haroutunian, B. Zhang, T. G. Beach, G. Yu, J. Peng, Deep Multilayer Brain Proteomics Identifies
676 Molecular Networks in Alzheimer's Disease Progression, *Neuron* **105**, 975-991.e7 (2020).

677 9. M. Perluigi, E. Barone, F. Di Domenico, D. A. Butterfield, Aberrant protein phosphorylation in
678 Alzheimer disease brain disturbs pro-survival and cell death pathways, *Biochim. Biophys. Acta*
679 **1862**, 1871–1882 (2016).

680 10. J. M. Axten, J. R. Medina, Y. Feng, A. Shu, S. P. Romeril, S. W. Grant, W. H. H. Li, D. A.
681 Heerding, E. Minthorn, T. Mencken, C. Atkins, Q. Liu, S. Rabindran, R. Kumar, X. Hong, A. Goetz,
682 T. Stanley, J. D. Taylor, S. D. Sigethy, G. H. Tomberlin, A. M. Hassell, K. M. Kahler, L. M.
683 Shewchuk, R. T. Gampe, Discovery of 7-methyl-5-(1-{[3-(trifluoromethyl)phenyl]acetyl}-2,3-
684 dihydro-1H-indol-5-yl)-7H-pyrrolo[2,3-d]pyrimidin-4-amine (GSK2606414), a potent and
685 selective first-in-class inhibitor of protein kinase R (PKR)-like endoplasmic reticulum kinase
686 (PERK), *J. Med. Chem.* **55**, 7193–7207 (2012).

687 11. H. Radford, J. A. Moreno, N. Verity, M. Halliday, G. R. Mallucci, PERK inhibition prevents tau-
688 mediated neurodegeneration in a mouse model of frontotemporal dementia, *Acta Neuropathol*
689 **130**, 633–642 (2015).

690 12. J. A. Moreno, M. Halliday, C. Molloy, H. Radford, N. Verity, J. M. Axten, C. A. Ortori, A. E.
691 Willis, P. M. Fischer, D. A. Barrett, G. R. Mallucci, Oral treatment targeting the unfolded protein
692 response prevents neurodegeneration and clinical disease in prion-infected mice, *Sci Transl*
693 *Med* **5**, 206ra138 (2013).

694 13. C. Meng, J. Zhang, B. Dang, H. Li, H. Shen, X. Li, Z. Wang, PERK Pathway Activation Promotes
695 Intracerebral Hemorrhage Induced Secondary Brain Injury by Inducing Neuronal Apoptosis Both
696 in Vivo and in Vitro, *Front Neurosci* **12** (2018), doi:10.3389/fnins.2018.00111.

697 14. T. Vanderweyde, D. J. Apicco, K. Youmans-Kidder, P. E. A. Ash, C. Cook, E. L. da Rocha, K.
698 Jansen-West, A. A. Frame, A. Citro, J. D. Leszyk, P. Ivanov, J. F. Abisambra, M. Steffen, H. Li, L.
699 Petrucelli, B. Wolozin, Interaction of tau with the RNA-Binding Protein TIA1 Regulates tau
700 Pathophysiology and Toxicity, *Cell Rep* **15**, 1455–1466 (2016).

701 15. V. Sharma, H. Ounallah-Saad, D. Chakraborty, M. Hleihil, R. Sood, I. Barrera, E. Edry, S. K.
702 Chandran, S. B. T. de Leon, H. Kaphzan, K. Rosenblum, Local Inhibition of PERK Enhances
703 Memory and Reverses Age-Related Deterioration of Cognitive and Neuronal Properties, *J.*
704 *Neurosci.* **38**, 648–658 (2018).

705 16. H. L. Smith, O. J. Freeman, A. J. Butcher, S. Holmqvist, I. Humoud, T. Schätzl, D. T. Hughes, N.
706 C. Verity, D. P. Swinden, J. Hayes, L. de Weerd, D. H. Rowitch, R. J. M. Franklin, G. R. Mallucci,
707 Astrocyte Unfolded Protein Response Induces a Specific Reactivity State that Causes Non-Cell-
708 Autonomous Neuronal Degeneration, *Neuron* **105**, 855-866.e5 (2020).

709 17. D. Rojas-Rivera, T. Delvaeye, R. Roelandt, W. Nerinckx, K. Augustyns, P. Vandenabeele, M. J.
710 M. Bertrand, When PERK inhibitors turn out to be new potent RIPK1 inhibitors: critical issues on
711 the specificity and use of GSK2606414 and GSK2656157, *Cell Death Differ* **24**, 1100–1110
712 (2017).

713 18. M. Mahameed, T. Wilhelm, O. Darawshi, A. Obiedat, W.-S. Tommy, C. Chintha, T. Schubert,
714 A. Samali, E. Chevet, L. A. Eriksson, M. Huber, B. Tirosh, The unfolded protein response
715 modulators GSK2606414 and KIRA6 are potent KIT inhibitors, *Cell Death Dis* **10**, 300 (2019).

716 19. Z. Berger, H. Roder, A. Hanna, A. Carlson, V. Rangachari, M. Yue, Z. Wszolek, K. Ashe, J.
717 Knight, D. Dickson, C. Andorfer, T. L. Rosenberry, J. Lewis, M. Hutton, C. Janus, Accumulation of
718 Pathological Tau Species and Memory Loss in a Conditional Model of Tauopathy, *J. Neurosci.* **27**,
719 3650–3662 (2007).

720 20. K. SantaCruz, J. Lewis, T. Spires, J. Paulson, L. Kotilinek, M. Ingelsson, A. Guimaraes, M.
721 DeTure, M. Ramsden, E. McGowan, C. Forster, M. Yue, J. Orne, C. Janus, A. Mariash, M.
722 Kuskowski, B. Hyman, M. Hutton, K. H. Ashe, Tau Suppression in a Neurodegenerative Mouse
723 Model Improves Memory Function, *Science* **309**, 476–481 (2005).

724 21. R. M. Bailey, J. Howard, J. Knight, N. Sahara, D. W. Dickson, J. Lewis, Effects of the C57BL/6
725 strain background on tauopathy progression in the rTg4510 mouse model, *Molecular*
726 *Neurodegeneration* **9**, 8 (2014).

727 22. S. N. Fontaine, A. Ingram, R. A. Cloyd, S. E. Meier, E. Miller, D. Lyons, G. K. Nation, E.
728 Mechas, B. Weiss, C. Lanzillotta, F. Di Domenico, F. Schmitt, D. K. Powell, M. Vandsburger, J. F.
729 Abisambra, Identification of changes in neuronal function as a consequence of aging and
730 tauopathic neurodegeneration using a novel and sensitive magnetic resonance imaging
731 approach, *Neurobiol Aging* **56**, 78–86 (2017).

732 23. R. A. Cloyd, S. A. Koren, J. F. Abisambra, Manganese-Enhanced Magnetic Resonance
733 Imaging: Overview and Central Nervous System Applications With a Focus on
734 Neurodegeneration, *Front Aging Neurosci* **10** (2018), doi:10.3389/fnagi.2018.00403.

735 24. B. T. Bedenk, S. Almeida-Corrêa, A. Jurik, N. Dedic, B. Grünecker, A. J. Genewsky, S. F.
736 Kaltwasser, C. J. Riebe, J. M. Deussing, M. Czisch, C. T. Wotjak, Mn2+ dynamics in manganese-
737 enhanced MRI (MEMRI): Cav1.2 channel-mediated uptake and preferential accumulation in
738 projection terminals, *NeuroImage* **169**, 374–382 (2018).

739 25. H. Lu, Z.-X. Xi, L. Gitajn, W. Rea, Y. Yang, E. A. Stein, Cocaine-induced brain activation
740 detected by dynamic manganese-enhanced magnetic resonance imaging (MEMRI), *Proc. Natl.*
741 *Acad. Sci. U.S.A.* **104**, 2489–2494 (2007).

742 26. H. Masumiya, H. Tsujikawa, N. Hino, R. Ochi, Modulation of manganese currents by 1, 4-
743 dihydropyridines, isoproterenol and forskolin in rabbit ventricular cells, *Pflugers Arch.* **446**, 695–
744 701 (2003).

745 27. K. Itoh, M. Sakata, M. Watanabe, Y. Aikawa, H. Fujii, The entry of manganese ions into the
746 brain is accelerated by the activation of N-methyl-d-aspartate receptors, *Neuroscience* **154**,
747 732–740 (2008).

748 28. M. H. Vandsburger, B. A. French, C. M. Kramer, X. Zhong, F. H. Epstein, Displacement-
749 encoded and manganese-enhanced cardiac MRI reveal that nNOS, not eNOS, plays a dominant
750 role in modulating contraction and calcium influx in the mammalian heart, *Am. J. Physiol. Heart*
751 *Circ. Physiol.* **302**, H412-419 (2012).

752 29. P. F. Antkowiak, M. H. Vandsburger, F. H. Epstein, Quantitative pancreatic β cell MRI using
753 manganese-enhanced Look-Locker imaging and two-site water exchange analysis, *Magn Reson*
754 *Med* **67**, 1730–1739 (2012).

755 30. F. M. LaFerla, Calcium dyshomeostasis and intracellular signalling in Alzheimer's disease,
756 *Nat. Rev. Neurosci.* **3**, 862–872 (2002).

757 31. C. Hooper, R. Killick, S. Lovestone, The GSK3 hypothesis of Alzheimer's disease, *J Neurochem*
758 **104**, 1433–1439 (2008).

759 32. M. C. Bell, S. E. Meier, A. L. Ingram, J. F. Abisambra, PERK-opathies: An Endoplasmic
760 Reticulum Stress Mechanism Underlying Neurodegeneration, *Curr Alzheimer Res* **13**, 150–163
761 (2016).

762 33. J. F. Abisambra, U. K. Jinwal, L. J. Blair, J. C. O'Leary, Q. Li, S. Brady, L. Wang, C. E. Guidi, B.
763 Zhang, B. A. Nordhues, M. Cockman, A. Suntharalingham, P. Li, Y. Jin, C. A. Atkins, C. A. Dickey,
764 Tau accumulation activates the unfolded protein response by impairing endoplasmic reticulum-
765 associated degradation, *J. Neurosci.* **33**, 9498–9507 (2013).

766 34. S. A. Koren, M. J. Hamm, S. E. Meier, B. E. Weiss, G. K. Nation, E. A. Chishti, J. P. Arango, J.
767 Chen, H. Zhu, E. M. Blalock, J. F. Abisambra, Tau drives translational selectivity by interacting
768 with ribosomal proteins, *Acta Neuropathol* **137**, 571–583 (2019).

769 35. S. B. Cullinan, D. Zhang, M. Hannink, E. Arvisais, R. J. Kaufman, J. A. Diehl, Nrf2 is a direct
770 PERK substrate and effector of PERK-dependent cell survival, *Mol. Cell. Biol.* **23**, 7198–7209
771 (2003).

772 36. L. O. Goodwin, E. Splinter, T. L. Davis, R. Urban, H. He, R. E. Braun, E. J. Chesler, V. Kumar, M.
773 van Min, J. Ndukum, V. M. Philip, L. G. Reinholdt, K. Svenson, J. K. White, M. Sasner, C. Lutz, S.
774 A. Murray, Large-scale discovery of mouse transgenic integration sites reveals frequent
775 structural variation and insertional mutagenesis, *Genome Res.* **29**, 494–505 (2019).

776 37. J. Gamache, K. Benzow, C. Forster, L. Kemper, C. Hlynialuk, E. Furrow, K. H. Ashe, M. D.
777 Koob, Factors other than hTau overexpression that contribute to tauopathy-like phenotype in
778 rTg4510 mice, *Nat Commun* **10**, 2479 (2019).

779 38. U. Raudvere, L. Kolberg, I. Kuzmin, T. Arak, P. Adler, H. Peterson, J. Vilo, g:Profiler: a web
780 server for functional enrichment analysis and conversions of gene lists (2019 update), *Nucleic*
781 *Acids Res* **47**, W191–W198 (2019).

782 39. B. Jassal, L. Matthews, G. Viteri, C. Gong, P. Lorente, A. Fabregat, K. Sidiropoulos, J. Cook, M.
783 Gillespie, R. Haw, F. Loney, B. May, M. Milacic, K. Rothfels, C. Sevilla, V. Shamovsky, S. Shorser,
784 T. Varusai, J. Weiser, G. Wu, L. Stein, H. Hermjakob, P. D'Eustachio, The reactome pathway
785 knowledgebase, *Nucleic Acids Res.* **48**, D498–D503 (2020).

786 40. P. Shannon, A. Markiel, O. Ozier, N. S. Baliga, J. T. Wang, D. Ramage, N. Amin, B.
787 Schwikowski, T. Ideker, Cytoscape: a software environment for integrated models of
788 biomolecular interaction networks, *Genome Res.* **13**, 2498–2504 (2003).

789 41. C. A. Goodman, T. A. Hornberger, Measuring protein synthesis with SUnSET: a valid
790 alternative to traditional techniques?, *Exerc Sport Sci Rev* **41**, 107–115 (2013).

791 42. D. A. Butterfield, T. T. Reed, M. Perluigi, C. De Marco, R. Coccia, J. N. Keller, W. R.
792 Markesbery, R. Sultana, Elevated Levels of 3-Nitrotyrosine in Brain From Subjects with Amnestic
793 Mild Cognitive Impairment: Implications for the Role of Nitration in the Progression of
794 Alzheimer's Disease, *Brain Res* **1148**, 243–248 (2007).

795 43. D. A. Butterfield, T. Reed, R. Sultana, Roles of 3-nitrotyrosine- and 4-hydroxynonenal-
796 modified brain proteins in the progression and pathogenesis of Alzheimer's disease, *Free Radic.*
797 *Res.* **45**, 59–72 (2011).

798 44. N. T. Seyfried, E. B. Dammer, V. Swarup, D. Nandakumar, D. M. Duong, L. Yin, Q. Deng, T.
799 Nguyen, C. M. Hales, T. Wingo, J. Glass, M. Gearing, M. Thambisetty, J. C. Troncoso, D. H.
800 Geschwind, J. J. Lah, A. I. Levey, A Multi-network Approach Identifies Protein-Specific Co-
801 expression in Asymptomatic and Symptomatic Alzheimer's Disease, *Cell Syst* **4**, 60-72.e4 (2017).

802 45. T. E. Golde, S. T. DeKosky, D. Galasko, Alzheimer's disease: The right drug, the right time,
803 *Science* **362**, 1250–1251 (2018).

804 46. L. Ping, D. M. Duong, L. Yin, M. Gearing, J. J. Lah, A. I. Levey, N. T. Seyfried, Global
805 quantitative analysis of the human brain proteome in Alzheimer's and Parkinson's Disease, *Sci*
806 *Data* **5**, 180036 (2018).

807 47. C. H. van Dyck, H. B. Nygaard, K. Chen, M. C. Donohue, R. Raman, R. A. Rissman, J. B.
808 Brewer, R. A. Koeppe, T. W. Chow, M. S. Rafii, D. Gessert, J. Choi, R. S. Turner, J. A. Kaye, S. A.
809 Gale, E. M. Reiman, P. S. Aisen, S. M. Strittmatter, Effect of AZD0530 on Cerebral Metabolic
810 Decline in Alzheimer Disease: A Randomized Clinical Trial, *JAMA Neurol* (2019),
811 doi:10.1001/jamaneurol.2019.2050.

812 48. S. Lovestone, M. Boada, B. Dubois, M. Hüll, J. O. Rinne, H.-J. Huppertz, M. Calero, M. V.
813 Andrés, B. Gómez-Carrillo, T. León, T. del Ser, ARGO investigators, A phase II trial of tideglusib in
814 Alzheimer's disease, *J. Alzheimers Dis.* **45**, 75–88 (2015).

815 49. E. Tolosa, I. Litvan, G. U. Höglinger, D. Burn, A. Lees, M. V. Andrés, B. Gómez-Carrillo, T.
816 León, T. Del Ser, TAUROS Investigators, A phase 2 trial of the GSK-3 inhibitor tideglusib in
817 progressive supranuclear palsy, *Mov. Disord.* **29**, 470–478 (2014).

818 50. M. Medina, An Overview on the Clinical Development of Tau-Based Therapeutics, *Int J Mol*
819 *Sci* **19** (2018), doi:10.3390/ijms19041160.

820 51. R. S. Turner, M. L. Hebron, A. Lawler, E. E. Mundel, N. Yusuf, J. N. Starr, M. Anjum, F. Pagan,
821 Y. Torres-Yaghi, W. Shi, S. Mulki, D. Ferrante, S. Matar, X. Liu, G. Esposito, F. Berkowitz, X. Jiang,
822 J. Ahn, C. Moussa, Nilotinib Effects on Safety, Tolerability, and Biomarkers in Alzheimer's
823 Disease, *Annals of Neurology* **88**, 183–194 (2020).

824 52. O. Hantschel, U. Rix, G. Superti-Furga, Target spectrum of the BCR-ABL inhibitors imatinib,
825 nilotinib and dasatinib, *Leuk. Lymphoma* **49**, 615–619 (2008).

826 53. T. L. Spires, J. D. Orne, K. SantaCruz, R. Pitstick, G. A. Carlson, K. H. Ashe, B. T. Hyman,
827 Region-specific Dissociation of Neuronal Loss and Neurofibrillary Pathology in a Mouse Model
828 of Tauopathy, *Am J Pathol* **168**, 1598–1607 (2006).

829 54. H. E. Holmes, N. Colgan, O. Ismail, D. Ma, N. M. Powell, J. M. O'Callaghan, I. F. Harrison, R. A.
830 Johnson, T. K. Murray, Z. Ahmed, M. Heggenes, A. Fisher, M. J. Cardoso, M. Modat, S. Walker-
831 Samuel, E. M. C. Fisher, S. Ourselin, M. J. O'Neill, J. A. Wells, E. C. Collins, M. F. Lythgoe, Imaging
832 the accumulation and suppression of tau pathology using multiparametric MRI, *Neurobiol Aging*
833 **39**, 184–194 (2016).

834 55. M. A. Busche, S. Wegmann, S. Dujardin, C. Commins, J. Schiantarelli, N. Klickstein, T. V.
835 Kamath, G. A. Carlson, I. Nelken, B. T. Hyman, Tau impairs neural circuits, dominating amyloid-β
836 effects, in Alzheimer models in vivo, *Nat Neurosci* **22**, 57–64 (2019).

837 56. T. Blackmore, S. Meftah, T. K. Murray, P. J. Craig, A. Blockeel, K. Phillips, B. Eastwood, M. J.
838 O'Neill, H. Marston, Z. Ahmed, G. Gilmour, F. Gastambide, Tracking progressive pathological
839 and functional decline in the rTg4510 mouse model of tauopathy, *Alzheimer's Research &*
840 *Therapy* **9**, 77 (2017).

841 57. C. Cook, J. H. Dunmore, M. E. Murray, K. Scheffel, N. Shukoor, J. Tong, M. Castanedes-Casey,
842 V. Phillips, L. Rousseau, M. S. Penuliar, A. Kurti, D. W. Dickson, L. Petrucelli, J. D. Fryer, Severe
843 amygdala dysfunction in a MAPT transgenic mouse model of frontotemporal dementia,
844 *Neurobiol. Aging* **35**, 1769–1777 (2014).

845 58. J. Lewis, E. McGowan, J. Rockwood, H. Melrose, P. Nacharaju, M. Van Slegtenhorst, K.
846 Gwinn-Hardy, M. Paul Murphy, M. Baker, X. Yu, K. Duff, J. Hardy, A. Corral, W. L. Lin, S. H. Yen,
847 D. W. Dickson, P. Davies, M. Hutton, Neurofibrillary tangles, amyotrophy and progressive motor
848 disturbance in mice expressing mutant (P301L) tau protein, *Nat. Genet.* **25**, 402–405 (2000).

849 59. H. Lee, G. Casadesus, X. Zhu, R. J. Castellani, A. McShea, G. Perry, R. B. Petersen, V. Bajic, M.
850 A. Smith, Cell Cycle Re-entry Mediated Neurodegeneration and Its Treatment Role in the
851 Pathogenesis of Alzheimer's Disease, *Neurochem Int* **54**, 84–88 (2009).

852 60. A. C. Hradek, H.-P. Lee, S. L. Siedlak, S. L. Torres, W. Jung, A. H. Han, H. Lee, Distinct
853 chronology of neuronal cell cycle re-entry and tau pathology in the 3×Tg-AD mouse model and
854 Alzheimer disease patients, *J Alzheimers Dis* **43**, 57–65 (2015).

855 61. C. Andorfer, C. M. Acker, Y. Kress, P. R. Hof, K. Duff, P. Davies, Cell-cycle reentry and cell
856 death in transgenic mice expressing nonmutant human tau isoforms, *J. Neurosci.* **25**, 5446–
857 5454 (2005).

858 62. M. C. Pace, G. Xu, S. Fromholt, J. Howard, K. Crosby, B. I. Giasson, J. Lewis, D. R. Borchelt,
859 Changes in proteome solubility indicate widespread proteostatic disruption in mouse models of
860 neurodegenerative disease, *Acta Neuropathol* **136**, 919–938 (2018).

861 63. W. Wan, S. Xia, B. Kalionis, L. Liu, Y. Li, The Role of Wnt Signaling in the Development of
862 Alzheimer's Disease: A Potential Therapeutic Target?, *Biomed Res Int* **2014** (2014),
863 doi:10.1155/2014/301575.

864 64. Y. Takaichi, Y. Ano, J. K. Chambers, K. Uchida, A. Takashima, H. Nakayama, Deposition of
865 Phosphorylated α-Synuclein in the rTg4510 Mouse Model of Tauopathy, *J. Neuropathol. Exp.*
866 *Neurol.* **77**, 920–928 (2018).

867 65. Y. Takaichi, J. K. Chambers, H. Inoue, Y. Ano, A. Takashima, H. Nakayama, K. Uchida,
868 Phosphorylation and oligomerization of α-synuclein associated with GSK-3β activation in the
869 rTg4510 mouse model of tauopathy, *Acta Neuropathol Commun* **8**, 86 (2020).

870 66. D. Twohig, H. M. Nielsen, α-synuclein in the pathophysiology of Alzheimer's disease, *Mol*
871 *Neurodegener* **14**, 23 (2019).

872 67. M. E. Larson, M. A. Sherman, S. Greimel, M. Kuskowski, J. A. Schneider, D. A. Bennett, S. E.
873 Lesné, Soluble α-synuclein is a novel modulator of Alzheimer's disease pathophysiology, *J.*
874 *Neurosci.* **32**, 10253–10266 (2012).

875 68. J. Modregger, B. Ritter, B. Witter, M. Paulsson, M. Plomann, All three PACSIN isoforms bind
876 to endocytic proteins and inhibit endocytosis, *J. Cell. Sci.* **113 Pt 24**, 4511–4521 (2000).

877 69. V. Anggono, K. J. Smillie, M. E. Graham, V. A. Valova, M. A. Cousin, P. J. Robinson, Syndapin I
878 is the phosphorylation-regulated dynamin I partner in synaptic vesicle endocytosis, *Nat.*
879 *Neurosci.* **9**, 752–760 (2006).

880 70. A. Braun, R. Pinyol, R. Dahlhaus, D. Koch, P. Fonarev, B. D. Grant, M. M. Kessels, B.
881 Qualmann, EHD proteins associate with syndapin I and II and such interactions play a crucial
882 role in endosomal recycling, *Mol. Biol. Cell* **16**, 3642–3658 (2005).

883 71. E.-M. S. Grimm-Günter, M. Milbrandt, B. Merkl, M. Paulsson, M. Plomann, PACSIN proteins
884 bind tubulin and promote microtubule assembly, *Exp. Cell Res.* **314**, 1991–2003 (2008).

885 72. Y. Liu, K. Lv, Z. Li, A. C. H. Yu, J. Chen, J. Teng, PACSIN1, a Tau-interacting protein, regulates
886 axonal elongation and branching by facilitating microtubule instability, *J. Biol. Chem.* **287**,
887 39911–39924 (2012).

888 73. F. Edlich, G. Fischer, Pharmacological targeting of catalyzed protein folding: the example of
889 peptide bond cis/trans isomerases, *Handb Exp Pharmacol* , 359–404 (2006).

890 74. L. J. Blair, B. A. Nordhues, S. E. Hill, K. M. Scaglione, J. C. O'Leary, S. N. Fontaine, L. Breydo, B.
891 Zhang, P. Li, L. Wang, C. Cotman, H. L. Paulson, M. Muschol, V. N. Uversky, T. Klengel, E. B.
892 Binder, R. Kayed, T. E. Golde, N. Berchtold, C. A. Dickey, Accelerated neurodegeneration
893 through chaperone-mediated oligomerization of tau, *J. Clin. Invest.* **123**, 4158–4169 (2013).

894 75. L. J. Blair, J. D. Baker, J. J. Sabbagh, C. A. Dickey, The emerging role of peptidyl-prolyl
895 isomerase chaperones in tau oligomerization, amyloid processing, and Alzheimer's disease, *J.*
896 *Neurochem.* **133**, 1–13 (2015).

897 76. U. K. Jinwal, J. Koren, S. I. Borysov, A. B. Schmid, J. F. Abisambra, L. J. Blair, A. G. Johnson, J.
898 R. Jones, C. L. Shults, J. C. O'Leary, Y. Jin, J. Buchner, M. B. Cox, C. A. Dickey, The Hsp90
899 cochaperone, FKBP51, increases Tau stability and polymerizes microtubules, *J. Neurosci.* **30**,
900 591–599 (2010).

901 77. J. Koren, U. K. Jinwal, Z. Davey, J. Kiray, K. Arulselvam, C. A. Dickey, Bending tau into shape:
902 the emerging role of peptidyl-prolyl isomerases in tauopathies, *Mol. Neurobiol.* **44**, 65–70
903 (2011).

904 78. J. Oroz, B. J. Chang, P. Wysoczanski, C.-T. Lee, Á. Pérez-Lara, P. Chakraborty, R. V. Hofele, J.
905 D. Baker, L. J. Blair, J. Biernat, H. Urlaub, E. Mandelkow, C. A. Dickey, M. Zweckstetter, Structure

906 and pro-toxic mechanism of the human Hsp90/PPIase/Tau complex, *Nat Commun* **9**, 4532
907 (2018).

908 79. J. J. Sabbagh, J. C. O'Leary, L. J. Blair, T. Klengel, B. A. Nordhues, S. N. Fontaine, E. B. Binder,
909 C. A. Dickey, Age-associated epigenetic upregulation of the FKBP5 gene selectively impairs
910 stress resiliency, *PLoS ONE* **9**, e107241 (2014).

911 80. C. L. Klaips, G. G. Jayaraj, F. U. Hartl, Pathways of cellular proteostasis in aging and disease,
912 *J. Cell Biol.* **217**, 51–63 (2018).

913 81. M. C. Inda, S. Joshi, T. Wang, A. Bolaender, S. Gandu, J. Koren Iii, A. Y. Che, T. Taldone, P.
914 Yan, W. Sun, M. Uddin, P. Panchal, M. Riolo, S. Shah, A. Barlas, K. Xu, L. Y. L. Chan, A. Gruzinova,
915 S. Kishinevsky, L. Studer, V. Fossati, S. A. Noggle, J. R. White, E. de Stanchina, S. Sequeira, K. H.
916 Anthoney, J. W. Steele, K. Manova-Todorova, S. Patil, M. P. Dunphy, N. Pillarsetty, A. C. Pereira,
917 H. Erdjument-Bromage, T. A. Neubert, A. Rodina, S. D. Ginsberg, N. De Marco Garcia, W. Luo, G.
918 Chiosis, The epichaperome is a mediator of toxic hippocampal stress and leads to protein
919 connectivity-based dysfunction, *Nat Commun* **11**, 319 (2020).

920 82. Y. Honjo, T. Ayaki, T. Horibe, H. Ito, R. Takahashi, K. Kawakami, FKBP12-immunopositive
921 inclusions in patients with α-synucleinopathies, *Brain Res.* **1680**, 39–45 (2018).

922 83. A. Deleersnijder, A.-S. Van Rompuy, L. Desender, H. Pottel, L. Buée, Z. Debyser, V.
923 Baekelandt, M. Gerard, Comparative analysis of different peptidyl-prolyl isomerases reveals
924 FK506-binding protein 12 as the most potent enhancer of alpha-synuclein aggregation, *J. Biol.*
925 *Chem.* **286**, 26687–26701 (2011).

926 84. M. Gerard, Z. Debyser, L. Desender, P. J. Kahle, J. Baert, V. Baekelandt, Y. Engelborghs, The
927 aggregation of alpha-synuclein is stimulated by FK506 binding proteins as shown by
928 fluorescence correlation spectroscopy, *FASEB J.* **20**, 524–526 (2006).

929 85. M. Gerard, Z. Debyser, L. Desender, J. Baert, I. Brandt, V. Baekelandt, Y. Engelborghs, FK506
930 binding protein 12 differentially accelerates fibril formation of wild type alpha-synuclein and its
931 clinical mutants A30P or A53T, *J. Neurochem.* **106**, 121–133 (2008).

932 86. M. Gerard, A. Deleersnijder, V. Daniëls, S. Schreurs, S. Munck, V. Reumers, H. Pottel, Y.
933 Engelborghs, C. Van den Haute, J.-M. Taymans, Z. Debyser, V. Baekelandt, Inhibition of FK506
934 binding proteins reduces alpha-synuclein aggregation and Parkinson's disease-like pathology, *J.*
935 *Neurosci.* **30**, 2454–2463 (2010).

936 87. F.-L. Liu, P.-H. Liu, H.-W. Shao, F.-L. Kung, The intracellular domain of amyloid precursor
937 protein interacts with FKBP12, *Biochem. Biophys. Res. Commun.* **350**, 472–477 (2006).

938 88. U. Kemmerling, P. Muñoz, M. Müller, G. Sánchez, M. L. Aylwin, E. Klann, M. A. Carrasco, C.
939 Hidalgo, Calcium release by ryanodine receptors mediates hydrogen peroxide-induced
940 activation of ERK and CREB phosphorylation in N2a cells and hippocampal neurons, *Cell Calcium*
941 **41**, 491–502 (2007).

942 89. S. E. Lehnart, F. Huang, S. O. Marx, A. R. Marks, Immunophilins and coupled gating of
943 ryanodine receptors, *Curr Top Med Chem* **3**, 1383–1391 (2003).

944 90. M. Forgac, Vacuolar ATPases: rotary proton pumps in physiology and pathophysiology, *Nat.*
945 *Rev. Mol. Cell Biol.* **8**, 917–929 (2007).

946 91. J. D. Pearson, D. B. DeWald, W. R. Mathews, N. M. Mozier, H. A. Zürcher-Neely, R. L.
947 Heinrikson, M. A. Morris, W. D. McCubbin, J. R. McDonald, E. D. Fraser, Amino acid sequence
948 and characterization of a protein inhibitor of protein kinase C, *J. Biol. Chem.* **265**, 4583–4591
949 (1990).

950 92. L. Wang, Y. Zhang, H. Li, Z. Xu, R. M. Santella, I. B. Weinstein, Hint1 inhibits growth and
951 activator protein-1 activity in human colon cancer cells, *Cancer Res.* **67**, 4700–4708 (2007).

952 93. O. Huber, J. Weiske, Beta-catenin takes a HIT, *Cell Cycle* **7**, 1326–1331 (2008).

953 94. N. Korsisaari, T. P. Mäkelä, Interactions of Cdk7 and Kin28 with Hint/PKCI-1 and Hnt1
954 histidine triad proteins, *J. Biol. Chem.* **275**, 34837–34840 (2000).

955 95. P. Liu, Z. Liu, J. Wang, X. Ma, Y. Dang, HINT1 in Neuropsychiatric Diseases: A Potential
956 Neuroplastic Mediator, *Neural Plast.* **2017**, 5181925 (2017).

957 96. M. P. Vawter, J. M. Crook, T. M. Hyde, J. E. Kleinman, D. R. Weinberger, K. G. Becker, W. J.
958 Freed, Microarray analysis of gene expression in the prefrontal cortex in schizophrenia: a
959 preliminary study, *Schizophr. Res.* **58**, 11–20 (2002).

960 97. M. P. Vawter, C. Shannon Weickert, E. Ferran, M. Matsumoto, K. Overman, T. M. Hyde, D. R.
961 Weinberger, W. E. Bunney, J. E. Kleinman, Gene expression of metabolic enzymes and a
962 protease inhibitor in the prefrontal cortex are decreased in schizophrenia, *Neurochem. Res.* **29**,
963 1245–1255 (2004).

964 98. Y. Fujiki, A. L. Hubbard, S. Fowler, P. B. Lazarow, Isolation of intracellular membranes by
965 means of sodium carbonate treatment: application to endoplasmic reticulum, *J. Cell Biol.* **93**,
966 97–102 (1982).

967 99. M. M. Savitski, T. Mathieson, N. Zinn, G. Sweetman, C. Doce, I. Becher, F. Pachl, B. Kuster,
968 M. Bantscheff, Measuring and managing ratio compression for accurate iTRAQ/TMT
969 quantification, *J. Proteome Res.* **12**, 3586–3598 (2013).

970 100. S. Meier, M. Bell, D. N. Lyons, J. Rodriguez-Rivera, A. Ingram, S. N. Fontaine, E. Mechas, J.
971 Chen, B. Wolozin, H. LeVine, H. Zhu, J. F. Abisambra, Pathological Tau Promotes Neuronal
972 Damage by Impairing Ribosomal Function and Decreasing Protein Synthesis, *J Neurosci* **36**,
973 1001–1007 (2016).

Acknowledgements: We thank the UF Proteomics and Mass Spectrometry core for proteomic analysis, the University of Kentucky Magnetic Resonance Imaging and Spectroscopy Center (MRISC) for MRI analysis. We thank Dr. Peter Davies for his generous contribution of the PHF1 antibody. We thank Dr. Fred Schmitt for insightful discussions and crucial intellectual contributions to this study. We thank Dr. Shelby Meier for her contributions to the work prior to this study and experimental support in this current project. **Funding:** This work was supported by the Alzheimer's Association NIRG-14-322441, Department of Defense AZ140097, NIH/NIMHD L32 MD009205-01, NIH 1R21NS093440, NIH/NINDS 1R01 NS091329-01. **Author Contributions:** S.A.K., S.N.F., and J.F.A. designed the project. S.A.K., M.J.H., R.C., S.N.F., C.L., J.R.R., A.I., M.B., E.J.M., S.M.G.E., N.Z., N.S., D.T., D.P., M.V., T.F., and A.M.S.H. performed experiments, acquired data, or assisted in analysis. S.A.K., M.J.H., and J.F.A drafted the manuscript. J.K., J.M.A., and N.J.L. edited the manuscript. **Competing interests:** GSK manufactured GSK2606414, which was used in this study. Moreover, this study was funded in part by a contract from GSK. JMA and NL are employed by GSK. **Data and materials availability:** Raw proteomic data will be accessible in PRIDE.

990 **Figures**

991

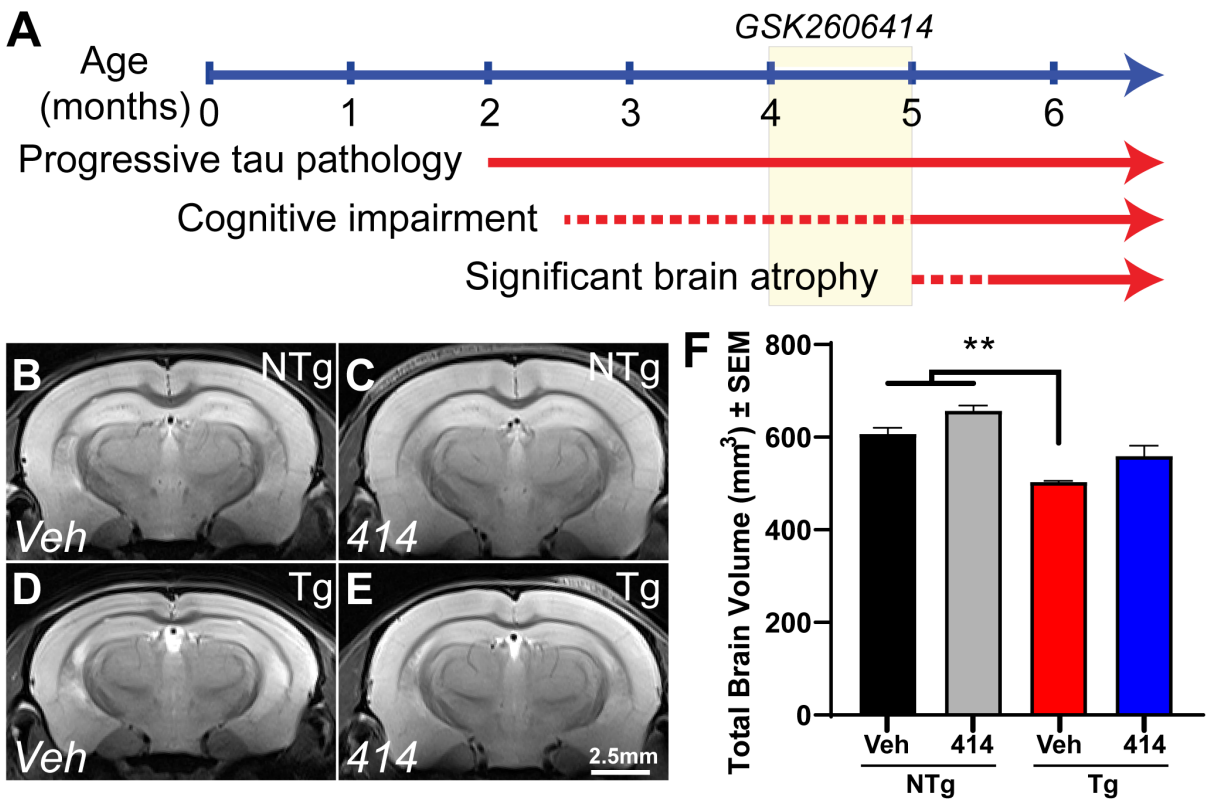

992

993 **Figure 1: Multi-target kinase inhibition with GSK2606414 rescues brain atrophy in rTg4510**
994 **tau transgenic mice.**

995 **A** Timeline of tauopathy phenotype in transgenic (Tg) mice and depiction of drug delivery between
996 4-5mo.

997 **B-E** Representative T2-weighted MR images of non-transgenic (NTg) and Tg mice treated with
998 vehicle (Veh) or GSK2606414 (414).

999 **F** Total brain volume quantification (NTg + 414, n = 2; others n = 3). Two-way ANOVA with
1000 Tukey *post hoc* test. Data are expressed as the mean ± SEM, $^{**}p < 0.01$.

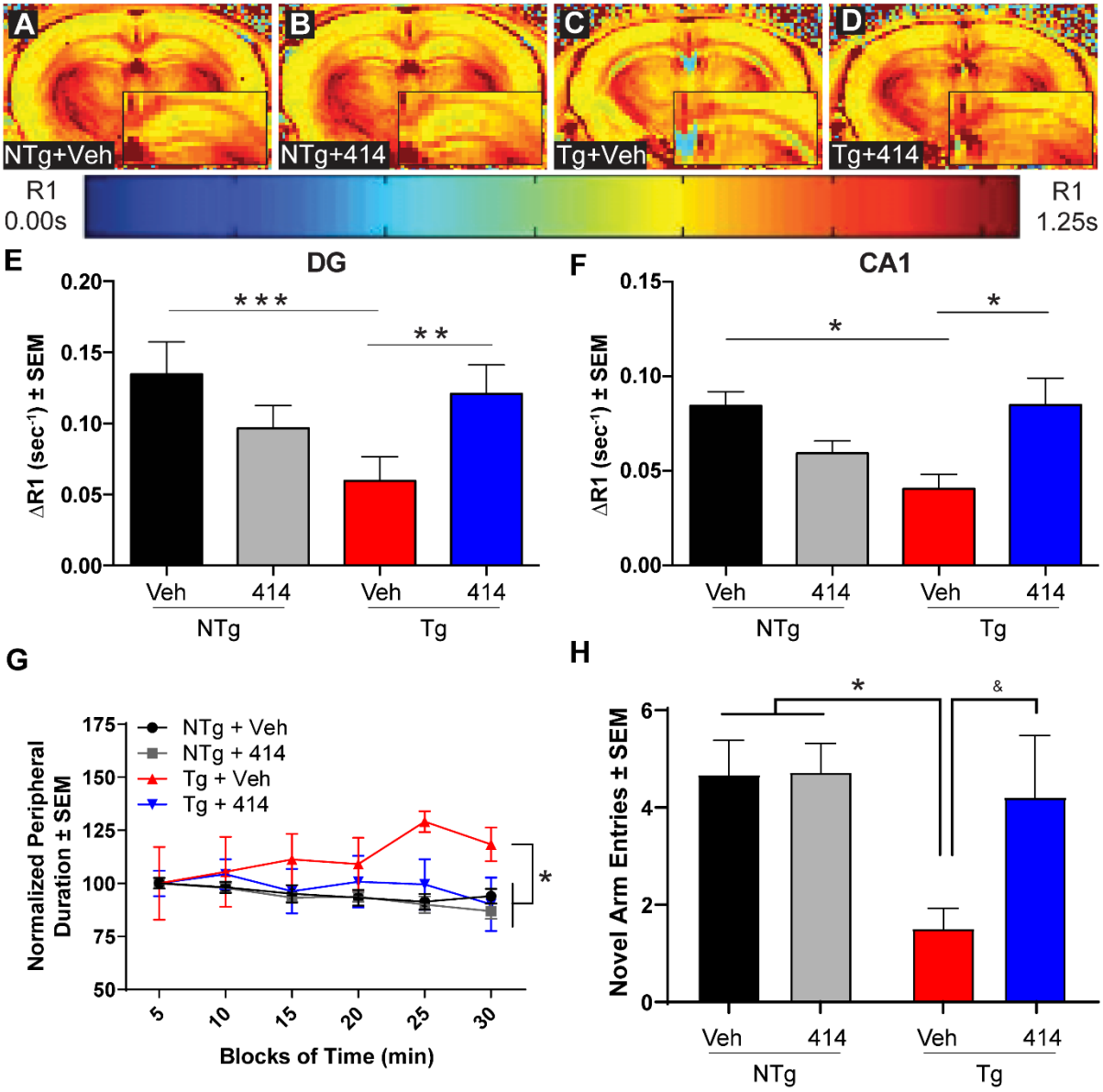

Figure 2: GSK2606414 treatment rescues brain dysfunction in tau transgenic mice.

A-D Representative ΔR1-rendered MEMRI images. The insets in panels A-D show half of the hippocampus of each representative image.

E-F Calculated ΔR1 values in the dentate gyrus (DG, **E**) and Cannu ammonis 1 (CA1, **F**). Two-way ANOVA with Tukey *post hoc* test. Data are expressed as the mean ± SEM, $*p < 0.05$, $**p < 0.01$, $***p < 0.001$, (n = 4-5).

G Results of open field behavioral task indicating percent of time spent in the periphery, normalized to the first five minutes (n = 6-10). Two-way ANOVA with Tukey *post hoc* test. Data are expressed as the mean relative to NTg + Veh ± SEM, $*p < 0.05$.

1011 **H** Y-maze behavioral task results for number of novel arm entries (n = 5-7). Two-way ANOVA
1012 with Tukey *post hoc* test. Data expressed as the mean ± SEM, *$p < 0.05$, & denotes p = 0.1095.

1013

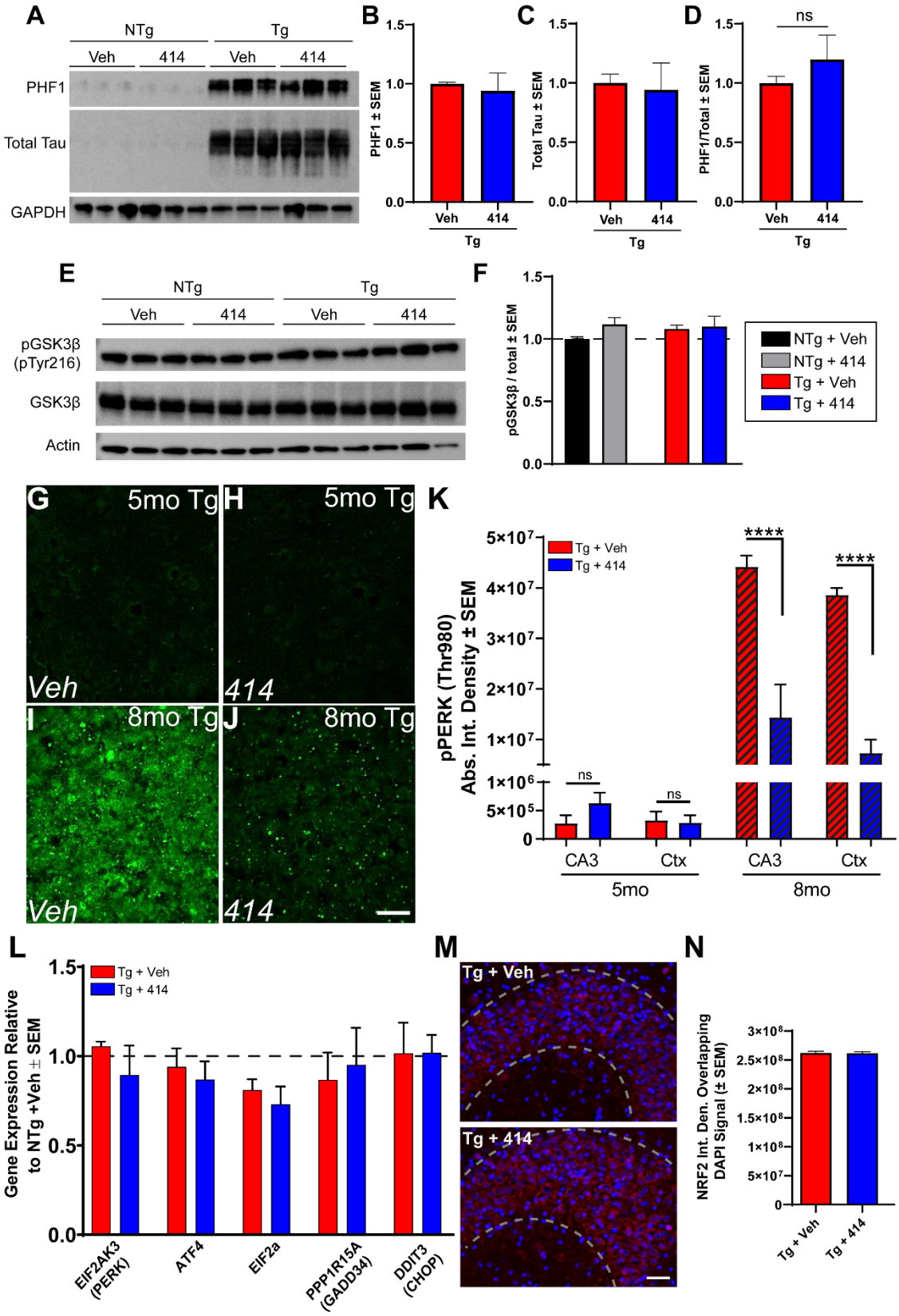
A
NTg
Tg
Veh
414
Veh
414
PHF1
Total Tau
GAPDH
B
PHF1 ± SEM
1.5
1.0
0.5
0.0
Veh
414
Tg
C
Total Tau ± SEM
D
ns
PHF1/Total ± SEM
E
pGSK3β (pTyr216)
GSK3β
Actin
F
pGSK3β / total ± SEM
NTg + Veh
NTg + 414
Tg + Veh
Tg + 414
G
5mo Tg
Veh
H
414
I
8mo Tg
J
K
pPERK (Thr980) Abs. Int. Density ± SEM
5×10⁷
4×10⁷
3×10⁷
2×10⁷
1×10⁷
1×10⁶
5×10⁵
0
****
ns
CA3
Ctx
5mo
8mo
L
Gene Expression Relative to NTg +Veh ± SEM
EIF2AK3 (PERK)
ATF4
EIF2a
PPP1R15A (GADD34)
DDIT3 (CHOP)
M
N
NRF2 Int. Den. Overlapping DAPI Signal (± SEM)
3×10⁸
2.5×10⁸
2×10⁸
1.5×10⁸
1×10⁸
5×10⁷

1014

1015 **Figure 3. GSK2606414-mediated cognitive rescue in early-stage tau transgenic mice is**
1016 **independent of tau hyper-phosphorylation and GSK3β activity**

1017 **A** Immunoblots of PHF1 (S396/S414) and total tau in 5mo NTg and Tg animals treated with
1018 vehicle or GSK2606414 (414).

1019 **B-D** Results of PHF1 (**B**), total tau (**C**), and relative phosphorylation (**D**) is normalized to GAPDH
1020 (n = 3). Two-way ANOVA with Tukey *post hoc* test. Data are expressed as the mean relative to
1021 Tg + Veh ± SEM.

1022 **E** Immunoblots of relative activated pY216 to total GSK3β level.
1023
1024 **F** Results of relative phosphorylation is provided normalized to actin (n = 3). Two-way ANOVA
1025 with Tukey *post hoc* test. Data are expressed as the mean relative to NTg + Veh ± SEM.
1026
1027 **G-J** Representative images of active, pT980 PERK (pPERK) staining. All images were post-
1028 processed equally and highlights lack of positive staining in 5mo Tg mice. Scale bar = 25 microns.

1029 **K** Quantification of pPERK staining reveals that 414 treatment has no detectable change in 5mo
1030 Tg mice (n = 5-7), but strongly inhibits PERK activity in the CA3 and superior medial cortex (Ctx)
1031 in 8mo Tg mice (hatched bars, n = 3). Two-way ANOVA with Sidak *post hoc* test. Data are
1032 expressed as the mean relative to NTg + Veh ± SEM, ****$p < 0.0001$.

1033 **L** Relative hippocampal gene expression of direct mediators of the PERK-UPR pathway in 5mo
1034 NTg and Tg mice treated for 30d with Veh or 414 normalized to GAPDH and 18S (n = 4-6). Two-
1035 way ANOVA with Tukey *post hoc* test. Data are expressed as the mean relative to NTg + Veh ±
1036 SEM, *$p < 0.05$, **$p < 0.01$.

1037 **M-N** Representative images (**M**) and quantification (**N**) of overlap between NRF2 (red) and
1038 nuclear staining (DAPI, blue) in the CA3 of 5mo NTg and Tg mice treated with either Veh or 414
1039 (n = 3). Unpaired Student's t-test. Error bars denote SEM. Scale bar = 25 microns.

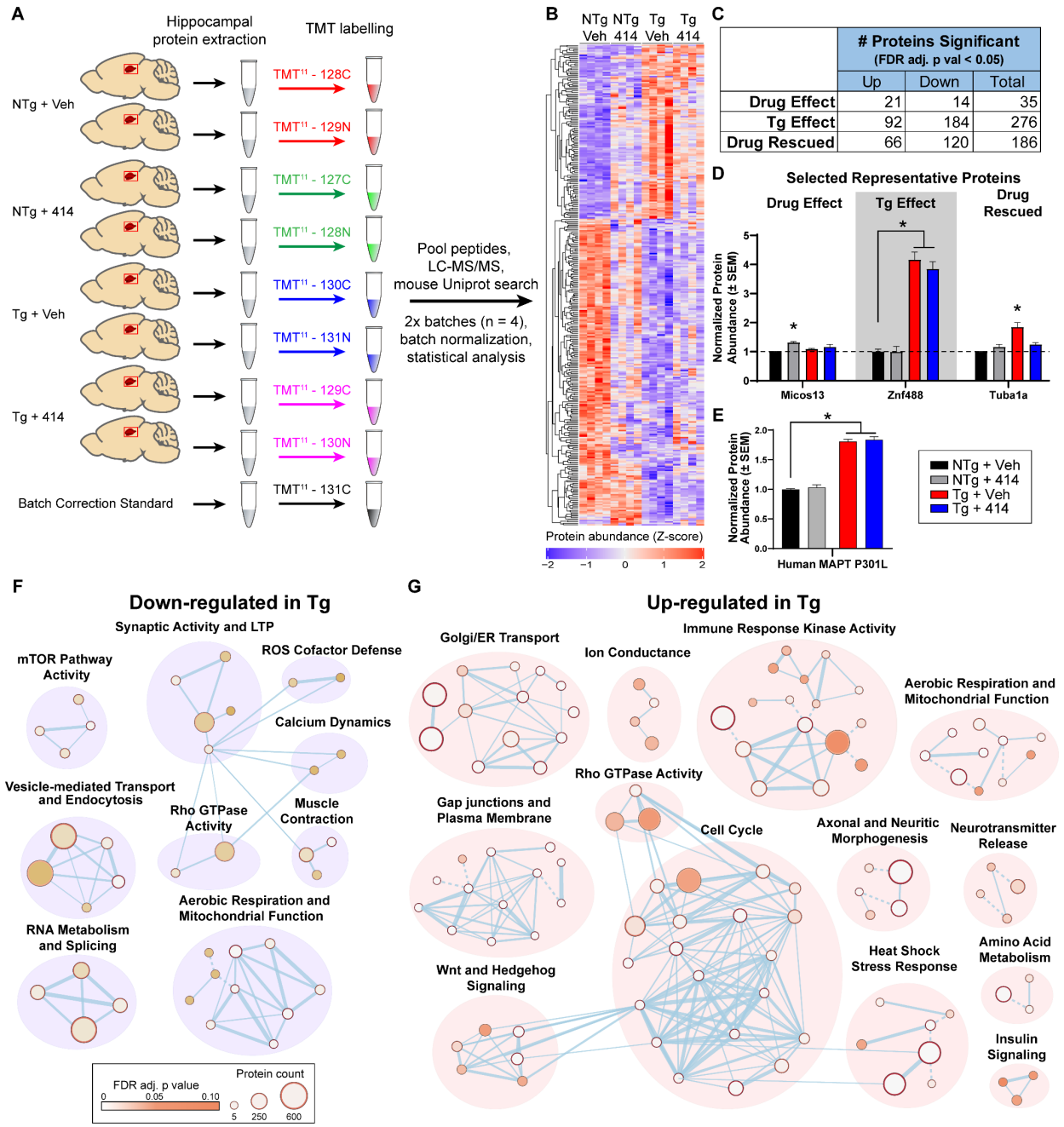

Figure 4. Hippocampal proteome signatures of early stage tauopathy model mice.

A Schematic of TMT isobaric tag proteomic pipeline. Mice hippocampal sections were extracted and lysed. Individual isobaric tags were used to chemically label proteins from each individual sample and combined for LC/MS-MS detection. Batch normalization was completed using a shared batch correction standard, resulting in n = 4 per group. All samples were from female mice.

B Heatmap of proteomics results showing 337 significantly altered proteins across all comparisons (FDR adjusted, $p < 0.05$).

C Summation of the number of significantly altered proteins across each test.

1049 **D** Representative protein for each test of significant differential abundance.

1050 **F-G** Network clustering of Reactome pathways found up-regulated (**F**) or down-regulated (**G**) due
1051 to tau transgenic genotype relative to NTg mice (Tg effect). Node size proportionally represents
1052 the protein count in that pathway, whereas node color represents the statistical significance
1053 gradient (FDR-adjusted p value) from p = 0.10 (brown) approaching p = 0 (white). Dashed
1054 connections indicate manually adjusted nodes.

1055

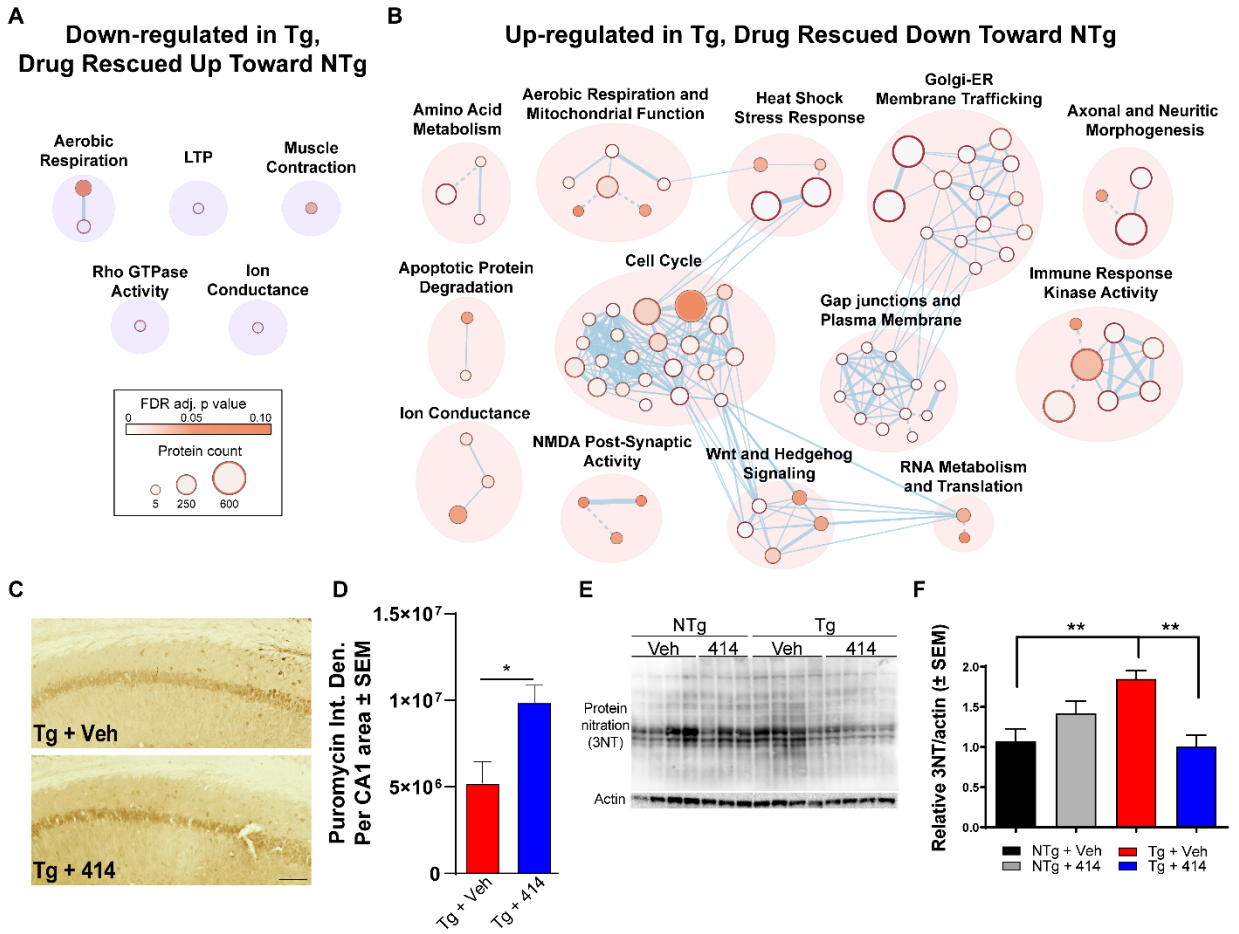

Figure 5. Multi-target kinase inhibition rescues pathways related to cognitive and neuronal function in early-stage tau transgenic mice.

A-B Network clustering of Reactome pathways found up-regulated (**F**) or down-regulated (**G**) in Tg mice and significantly rescued toward NTg + Veh levels in Tg + 414 mice. Node size proportionally represents the protein count in that pathway, whereas node color represents the statistical significance gradient (FDR-adjusted p value) from p = 0.10 (brown) approaching p = 0 (white). Dashed connections indicate manually adjusted nodes.

C-D Puromycin immunostaining of the CA1 region (**D**) and quantified (**E**) relative to total CA1 area (n = 3). One-way ANOVA with Tukey *post hoc* test. Data are expressed as the mean absolute integrated density ± SEM, *p < 0.05. Scale bar = 25 microns.

E-F Immunoblots (e) of total tyrosine nitration and total lane quantified results (**F**) relative to NTg + Veh and normalized to actin (n = 3 - 4). Two-way ANOVA with Tukey post hoc test. Data are expressed as the mean relative to Tg + Veh ± SEM, **p < 0.01.

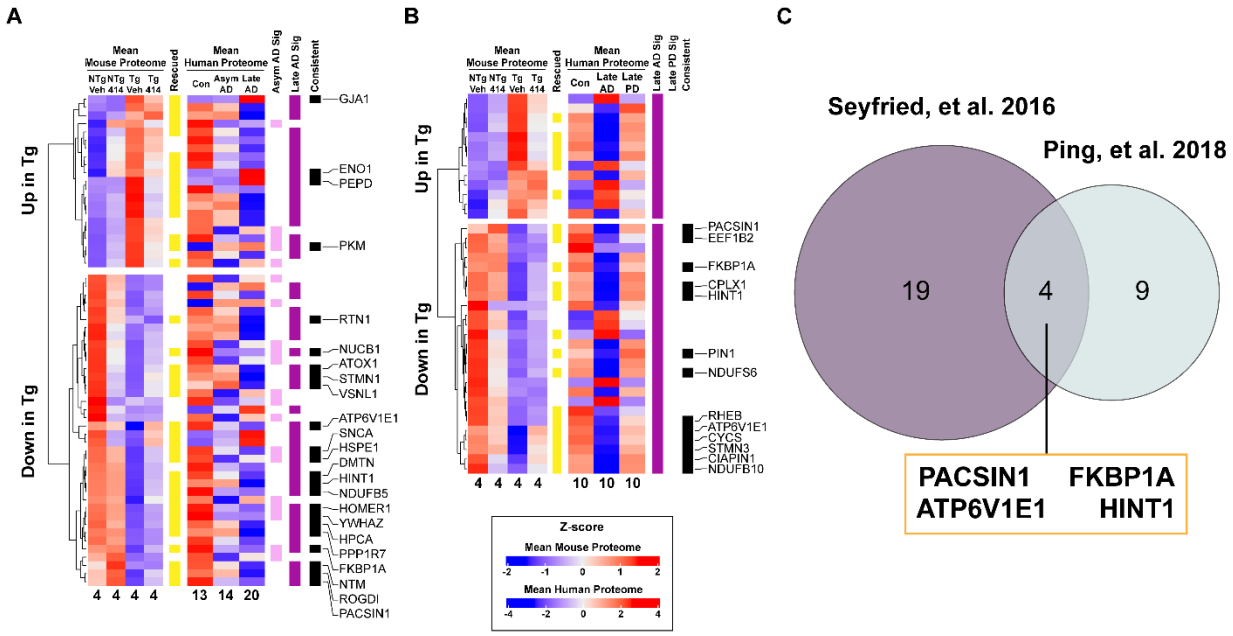

Figure 6: Proteomic signatures of rTg4510 transgenic mice match human tauopathy and reveal novel candidates for therapeutic intervention.

A-B Significantly altered proteins by Tg effect were compared to human homolog abundances found in two proteomics analyses of human neurodegenerative diseases (**A**, Seyfried et al., 2016; **B**, Ping et al., 2018). Proteins annotated in the "Rescued" column (yellow) were significantly rescued by 414 in Tg animals compared to NTg controls. Human homolog protein abundances in each human disease group were compared to non-demented controls. Statistically different human proteins were annotated by disease group in different colors (Asym AD, pink; late AD, purple; late PD, green). Proteins that were significantly altered in the same direction (increased or decreased) between species were annotated in the "Consistent" column (black). Candidate proteins passing all criteria for inclusion were labeled with their corresponding human gene symbols. Sample abundances were averaged per group and each corresponding sample number was appended to the bottom of each column.

C Venn diagram comparing candidate proteins identified in late AD across both datasets.

Supplementary Figures:

SFig. 1

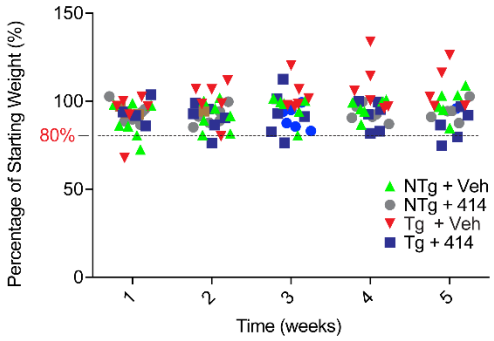

SFig. 2

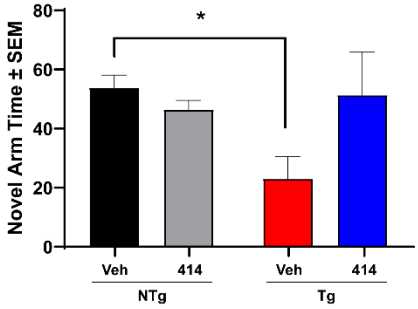

SFig. 3

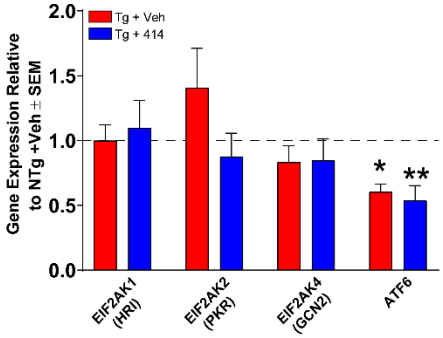

Fig. S1. Total duration spent in novel arm is partially rescued in tau transgenic mice treated with GSK2606414. Total time was measured during mouse exploration in the Y-maze behavioral task. Tg + Veh mice exhibited reduced time spent in the novel arm (*p = 0.0433). Tg mice treated with 414 were only partially rescued compared to Tg + Veh mice (p = 0.0882). Data were compared using two-way ANOVA with Tukey *post hoc* test.

Fig. S2. Non-PERK UPR proteins do not have altered transcript levels in 5mo tau transgenic mice. Other eIF2a kinases do not have altered transcript levels in 5mo Tg mice. *ATF6* transcript levels decrease in Tg mice compared to NTg controls, though 414 has no effect. Transcript levels normalized to GAPDH and 18S (n = 4-6). Two-way ANOVA with Tukey *post hoc* test. Data are expressed as the mean relative to NTg + Veh ± SEM, *$p < 0.05$, **$p < 0.01$.

1105 **Fig. S3. GSK2606414 treatment for 30d does not cause marked weight loss.** Prolonged
1106 treatment with GSK2606414 induces weight loss in mice *(12)*. However, treatment for only 30d
1107 was not sufficient to alter weight loss using a 100mg/kg treatment paradigm.
1108
1109 **Table S1. Top kinase targets of GSK2606414 and relevance to tauopathy.**

1110 The top targets of GSK2606414 with experimentally determined IC50 are listed based on
1111 reported data *in vitro (10)* or based on cell culture experiments *(17, 18)*. Relevance to tauopathy
1112 is briefly summarized.

1113 **Table S2. Significantly enriched reactome pathways identified by proteomics.** Reactome
1114 pathways significantly altered (FDR adjusted $p < 0.10$) by either direction in Tg mice compared
1115 to NTg controls along with pathways determined rescued by 414.

1116 **Table S3. Human to mouse proteomic comparisons.**

1117 **Table S4. Patient demographics of human proteomic samples.**

1118 Patient demographics and disease-related pathology scores were averaged and compiled from
1119 original reports *(44, 46)*.
1120